Catena 268 (2026) 110058

Contents lists available at ScienceDirect

Catena

journal homepage: www.elsevier.com/locate/catena

Ancient and recent soils as indicators of the genesis and evolution of Salada de Chiprana from middle Pleistocene to present (Ebro Basin, NE Spain)

M. Tierra [a], C. Castañeda [a,*], F.J. Gracia [b], R. Rodríguez-Ochoa [c], J.R. Olarieta [c], A. Medialdea [d], O. Castillo [e]

[a] Estación Experimental de Aula Dei, EEAD-CSIC, Ave. Montañana 1005, 50059 Zaragoza, Spain
[b] Dpt. Earth Sciences, Faculty of Marine and Environmental Sciences, University of Cádiz, 11510, Puerto Real, Cádiz, Spain
[c] Dpt. Química, Física y Ciencias Ambientales y del Suelo, Escuela Técnica Superior de Ingeniería Agroalimentaria y Forestal y de Veterinaria, University of Lleida, Ave. Rovira Roure 191, 25198 Lleida, Spain
[d] Centro Nacional de Investigación sobre la Evolución Humana, CENIEH, Paseo Sierra de Atapuerca 3, 09002 Burgos, Spain
[e] Dpt. Ingeniería Industrial e Ingeniería Civil, University of Cádiz, Campus Bahía de Algeciras, Ave. Ramón Puyol s/n 11202 Algeciras, Cádiz, Spain

ARTICLE INFO

Dataset link: Soils and geomorphology of "Salada de Chiprana" RAMSAR wetland, NE Spain (Original data)

Keywords:
Aeolian deposits
Ebro Basin
Endorheism
Middle Pleistocene
Saline wetland
Silt-clay dune
Optically stimulated luminescence (OSL)

ABSTRACT

The multidisciplinary study of soils, past and present, and the deposits around the Salada de Chiprana Lake (Central Ebro Basin, Spain) has provided valuable insights into the genesis of the lake, with important palaeoenvironmental and palaeoclimatic implications. The presence of a Middle Pleistocene (322.2 ± 21.6 ka) palaeosoil developed on perched aeolian deposits (CHI2) near the lake shore is evidence of ancient stages of lake bottom exposition under rather arid conditions, representing one of the oldest dated aridification episodes in the Quaternary of the Ebro Basin, coinciding with cold periods. Texture analysis of the soils and deposits, and the application of wind models to the reconstruction of the palaeowinds responsible for its genesis, helped to reconstruct the origin and conditions under which such deposits and soils developed. Regarding the genesis of the depression, the characteristics of the geological units in the lake basin, the relationship of the lake basin with fluvial terraces of the surrounding rivers, and the present morphology of the lake body, together with other indirect morphological indicators, point to the subsurface evacuation of soft sediments, very likely through piping-related processes. Additionally, a second soil (CHI1) was studied on a lacustrine terrace level at 152 m a.s.l., 8 m higher than the current level of the lake. It was dated at 9.0 ± 0.7 ka and corresponds to a period of more severe flooding of the lake during the early Holocene, an interpretation consistent with previous studies that established a Holocene age for the bottom sediments of the current lake. Altogether, our dataset indicates long-standing persistence of this lacustrine system and confirms its highly fluctuating character, typical of semiarid regimes such as the one that currently prevails in the centre of the Ebro Depression.

1. Introduction

Sedimentological and geochemical data obtained from lake records are invaluable for reconstructing palaeoenvironmental conditions and climatic changes along the Quaternary. However, despite the diverse information derived from their analysis (González-Sampériz et al., 2008; Martín-Puertas et al., 2010; Gutiérrez et al., 2013), the interpretation very commonly refers to data obtained from only one dimension; the one corresponding to the borehole excavated from the lake sediments. A large number of boreholes are needed to cover enough area to provide the necessary information for a more reliable paleogeographical reconstruction (McGlue et al., 2013; Hage et al., 2017), which would undoubtedly increase the required budget. It is important to highlight the need for a detailed geomorphological framework and information on the soil processes that have impacted these sedimentary records.

Shallow lakes in semiarid environments are usually highly fluctuating. High-level episodes produce coastal sedimentary accumulations that are left behind during low level stages. Past, perched deposits can be preserved in a number of forms: stepped terraces (Hare et al., 2001), abandoned littoral ridges, spits and beaches (McFadden et al., 1992; Søe et al., 2018), and associated soils (Mermut and Acton, 1984). Their forms and characteristics can be very useful for the reconstruction of

* Corresponding author.
E-mail address: ccastaneda@eead.csic.es (C. Castañeda).

https://doi.org/10.1016/j.catena.2026.110058
Received 26 May 2025; Received in revised form 28 January 2026; Accepted 23 March 2026
Available online 31 March 2026

lake extension, depth, and associated geological materials in past high-level episodes (Castañeda and Gracia, 2017), for the estimation of paleowinds (Adams, 2003; Wang et al., 2017), or for the analysis of past lake coast dynamics (May et al., 2022; Gracia et al., 2023).

The widespread occurrence of endorheic depressions in the semiarid Ebro Basin (NE Spain) includes a significant number of lakes varying in size, either isolated or grouped forming lake fields (Ibáñez, 1973, 1976; Van Zuidam, 1976; Castañeda et al., 2005; Gutiérrez and Gutiérrez, 2014). Most of them are playa-lakes, with highly variable water levels including periods of complete desiccation. Apart from climate, the endorheism of the Ebro Basin is marked by morphological and lithological factors, like low topography, or the prevalence of impervious outcropping rocks, many of which are soluble like gypsums and other evaporites (Dantín, 1942, Ibáñez, 1975). Closed depressions are mainly caused by dissolution together with wind or hydroaeolian erosion (Quirantes, 1969; Ibáñez, 1975; Sánchez-Navarro et al., 1998; Gutiérrez and Peña, 1993; Gutiérrez et al., 2005, 2013). In some cases, the genesis of lakes in the Ebro Basin is not evident and other factors have been adduced, such as aeolian erosion or the role of groundwater inflow to evaporation points (Ibáñez, 1975; Sánchez-Navarro et al., 1998). Studies by other research groups have mostly focused on the genesis of the depressions and their historical evolution, mainly during the Holocene, through the analysis of sediment cores (Moreno et al., 2012; Gutiérrez et al., 2013) or with satellite imagery (Castañeda et al., 2005). However, few lakes in this region have been evaluated through the study of the associated soils and their combination with other related approaches, like geomorphology and sedimentology (Castañeda et al., 2015, 2017; Luna et al., 2016; Gracia et al., 2021).

Castañeda and García-Vera (2008) studied the hydrology of a high number of small lakes and in the Monegros playa-lakes (central Ebro Basin), mostly excavated in soluble Miocene gypsum and limestone. These authors concluded that the hydrology of the lakes also depends on groundwater discharge, which makes them exhibit strong water level and salinity fluctuations. The exceptions are former playa-lakes that are now permanent fresh water lakes due to irrigation return flows (like Sariñena Lake; Castañeda et al., 2017) or water from irrigation channel networks (like Estanca de Alcañiz or Las Roces lakes; Anento and Ponz, 1992; Jódar et al., 2020). Some closed depressions in the Ebro Basin provided new insights into this genetic scheme: The multidisciplinary study of Sariñena Lake (Castañeda et al., 2017) revealed that piping-related processes were determinant in its generation and evolution. In summary, the different genetic models proposed for the lacustrine depressions in the Ebro Basin basically include karst dissolution and related groundwater processes, aeolian erosion, and piping.

Instead, the origin of some other lakes still remains unknown. This is the case with Chiprana Lake ("Salada de Chiprana"), the only permanent hypersaline lake in the central Ebro Basin (Doyle et al., 2022a). This has only received attention during the last few decades due to its environmental-ecological (Microbial mats; Guerrero et al., 1991) and scenic relevance. According to Ibáñez (1976), the origin of the lake is related to differential erosion, supposedly aeolian erosion. Davis Davis (1994) and Valero-Garcés et al. (2000) reconstructed the Holocene and historical evolution of the lake from an original playa-lake, on the basis of a 1.7 m deep borehole located in the centre of the lake, without providing any genetic model of the depression. The shape of the lake and other minor closed depressions nearby, their location in a zone seemingly protected from the prevailing winds, and the mainly non-karstifiable substratum make us priori discard wind erosion as the main process responsible for its generation. However, diverse Quaternary deposits of a different nature, identified in its surrounding rims and linked to the lake, and specially the soils developed on them, can provide clues as to the genesis of the depression and its evolution.

Most geolimnological work recently carried out in the Ebro Basin and especially in Chiprana Lake has focused on the nature of the sediments accumulated in the lake bottoms and their relationship to palaeoenvironmental forcing, especially regarding recent evolution (Valero-Garcés et al., 2000; González-Sampériz et al., 2008; De Wit et al., 2013). Aeolian processes and differential erosion are usually cited as a way of explaining the presence of such depressions in the Ebro Basin, without analysing in depth the causes and detailed genesis of the lakes. In this sense, during the last decades few studies have addressed the origin of the lake. In order to cover this gap of regional relevance, the present work aims to solve such questions as: How was this closed depression generated?, when did it happen?, when did lacustrine conditions settle to become a permanent lake?, and what was the role of wind and karst in the genesis and evolution of the closed depression? The answers to all these questions would provide important information regarding the Quaternary climatic and environmental evolution of the central Ebro Basin This requires applying several methods of a different nature that may converge to reconstruct the genesis and evolution of this lacustrine system. The present work includes the study of soils associated with lacustrine-linked deposits, together with geomorphological mapping, sedimentology of the accumulations and absolute dating. The combination of all these methods and techniques is used to build a conceptual model about the genesis and evolution of this peculiar case of endorheic depression in the Ebro Basin and its implications in the reconstruction of the Quaternary climate evolution at a regional scale.

2. Geographical background

The Ebro Basin (NE Spain) is surrounded by the Pyrenean Range to the north, the Iberian Range to the southwest and the Catalan Coastal Range to the east, and is drained by the River Ebro to the Mediterranean Sea. The study area is located in the semiarid central area, close to the River Ebro (Fig. 1), where the meanders are confined by Neogene morphostructures, mainly limestone platforms and sandstone ribbons, which limit any rapid incision of the valley during the Quaternary (Quirantes, 1969). A secondary valley, Regallo Creek, is located to the East of Chiprana Lake, running to the NE until reaching a meander of the River Ebro at 114 m a.s.l., 2 km away from the lacustrine complex.

Data from the nearest weather station at Caspe village, located 11 km to the east of Chiprana, characterises the area with a mean annual temperature of 15.8 °C, a maximum of 44.7 °C, an annual rainfall from 191 mm to 484 mm (mean of 316.4 mm for the period 2004–2024), and a mean annual evapotranspiration of 1500 mm (Smith et al., 1990). The predominant regional wind direction in the Ebro Basin is NW (Ortega et al., 2022). Híjar weather station, located 23 km to the SW in a more exposed area, shows prevalent winds from the W-NW (Fig. 2a). However, Caspe weather station shows predominant winds coming from a more westerly direction (Fig. 2b). In both cases westerly winds exceed 30% of frequency, and their velocity broadly ranges between 1.4 and 13.9 m s^{-1} About 30% of the westerly winds in the zone are dry and linked to a rainfall intensity of less than 2 mm per day.

The lithology of the area is characterized by an Oligo-Miocene geological unit formed by shales, sandstones of fluvial origin forming ribbons, and subordinate levels of limestones and evaporites. This unit consists of middle and distal alluvial deposits of an ancient fluvial system developed during the Neogene endorheic phase of the Ebro Basin (Cuevas et al., 2010). The resulting landscape is formed by a network of exhumed sandstone protrusions and ribbons associated with paleochannels. These form a complex network of elongated rocky outcrops separated by shallow depressions and valleys excavated on marls and clays due to differential erosion. The length and width of the sandstone ribbons vary from just a few meters to 15 m, and their height is usually less than 2 m. Their irregular distribution is responsible for the intricate patination of the present Chiprana Lake shore (Fig. 1b and c). While sandstones prevail in the western, hilly area, the relative abundance of clays increases towards the East.

Chiprana Lake, located in a relatively flat area at 138 m a.s.l., has been included in the Ramsar List (Ramsar Convention Secretariat, 2010) since 1999 and in Natura 2000 protected areas (ES2430041). Chiprana is the main water body of a wider lacustrine complex, the "Complejo

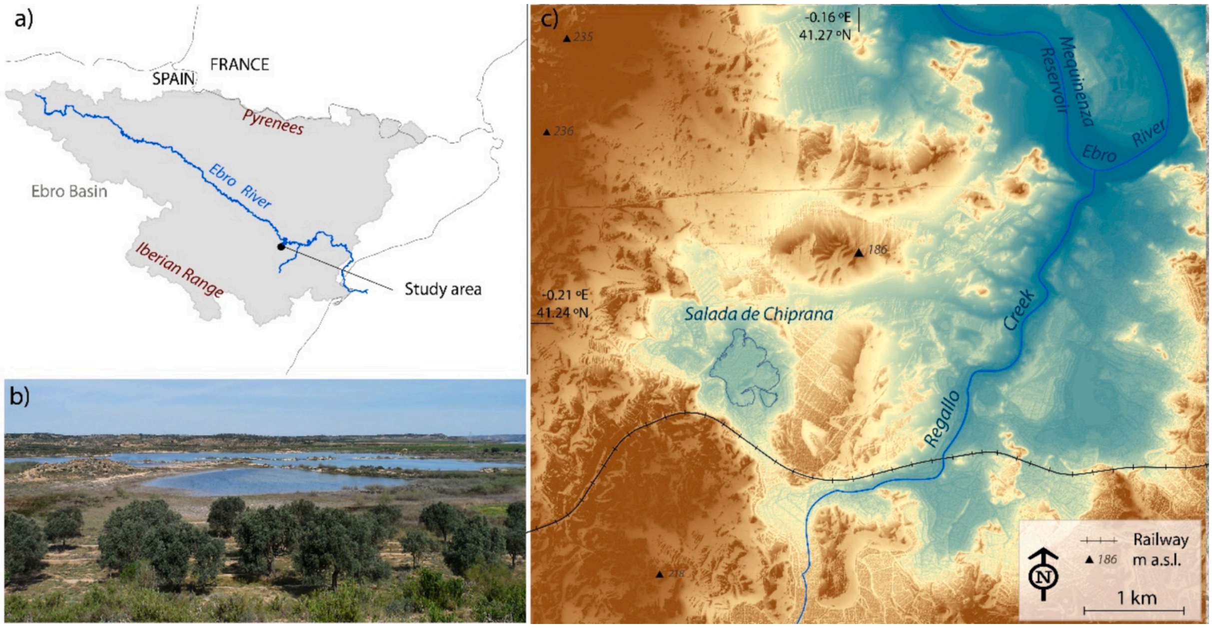

Fig. 1. Geographical setting of the study zone. a) Location of the Chiprana Lake in the Ebro Basin (in gray); b) Chiprana Lake in April 2023, c) Digital Elevation Model from PNOA data set (LiDAR-PNOA-cob2 2015 CC-BY 4.0 (scne.es)).

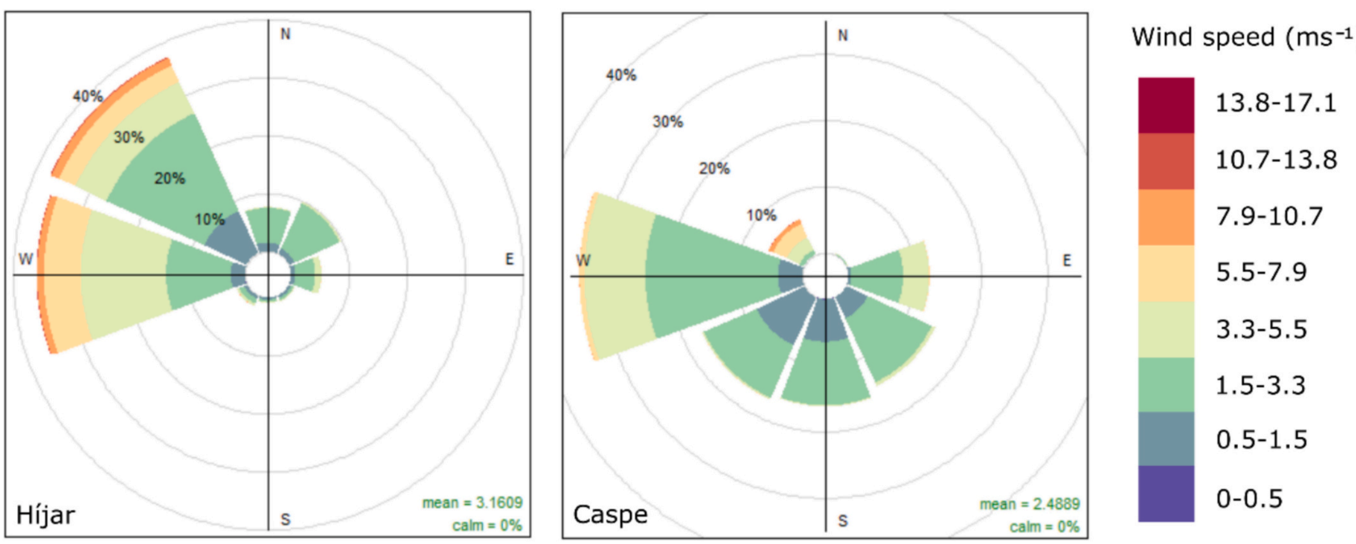

Fig. 2. Percentage of wind frequency by direction obtained from Híjar (left) and Caspe (right) weather stations for the period 2004–2024. Data from the Spanish Agroclimatic Information System for Irrigation (SIAR), https://eportal.mapa.gob.es/websiar/Inicio.aspx.

Lagunar de Chiprana", or Chiprana lacustrine basin, a permanent hypersaline wetland system (Doyle et al., 2022a), formed by several depressions. The biggest body of water, which gives name to the complex, has a relatively variable water surface to the extent of about 41 ha, and a maximum registered water depth of 5.6 m (Guerrero et al., 1991). Chiprana is fed both by the regional groundwater from the Iberian Range and by rainfall (Jódar et al., 2020). The water salinity is variable depending on the season, the water depth, and the sample location. The electrical conductivity (EC), documented by previous studies, can range from 27 dS m^{-1} at 25 °C (Vidondo and Guerrero, 1992) to 47 dS m^{-1} at 25 °C (Doyle et al., 2022b), and it can reach 150 dS m^{-1} during the dry season (own unpublished data from October 2025). Under the water column or the salt crust, the soil redox conditions (ORP) can vary from −140 mV to −450 mV (own unpublished data) favouring the formation of sulfures (black layers) due to sulfate reduction. The ionic composition of the water is characterized by the predominance of sulfate and chloride together with sodium and magnesium (Pueyo, 1978–79, Doyle et al., 2022b). Occasionally, controlled fresh water inputs from two irrigation ditches help to maintain the level of the lake. Close to Chiprana Lake two smaller depressions stand out: Prado del Farol, currently dry, and Salada de las Roces, presently a 3 m deep permanent fresh water lake, communicated with Chiprana through an ancient narrow channel excavated in the rocky substratum. The recent, historical evolution of Chiprana Lake (from the 19th century onwards) based on boreholes made along the lake bottom revealed the persistent tendency of the lake to water level fluctuations, with episodes of high water and extensive charophyte development alternating with dry periods with predominant gypsum precipitation.

3. Materials and methods

3.1. Geomorphological mapping

Quaternary deposits and structural, lacustrine and fluvial forms were mapped through stereoscopic photointerpretation, applied to aerial photographs of a USAF flight (1956–57) at 1:33,000 scale accompanied by field inspections. A detailed vertical ortophotograph (OrtoPNOA 2021 CC-BY 4.0, scene.es) with a pixel size of 35 cm was used to identify small cartographic units. The USAF geomorphological interpretation made on acetate film was digitized and georeferenced within the geographic information system ArcGIS© (v.10.8.2). LiDAR-PNOA-cob2 2015 CC-BY 4.0 (scne.es) was used with a density of 0.5 points m^{-2} to complement the geomorphological photointerpretation.

3.2. Soil description and sampling, and laboratory procedures

The main study was focused on soils from selected landforms and deposits identified in the geomorphological map and during field inspections as representative of different outstanding (lacustrine) processes. In September 2023 a pit, down to groundwater level, at a depth of 180 cm, was opened in the lacustrine terrace (pedon CH1, 41.24°N, −0.17°W), and another was opened to a depth of 200 cm and augered to a depth of 300 cm in one of the aeolian deposits (pedon CH2, 41.23°N, −0.18°W). The pedons were described (Schoeneberger et al., 2012) and classified following Soil Taxonomy (Soil Survey Staff (SSS), 2022). A total of 25 soil samples representative of genetic horizons and of the soil surface crust in CHI1 were collected.

In the laboratory, samples were dried at room temperature, ground and sieved through a 2-mm mesh. Soil salinity was measured as the electrical conductivity of the 1:5 water:soil extract (EC 1:5) and in the saturated paste extract (ECe) (MAPA, 1994) using a conductivity cell (Orion 013605MD) and expressed in dS m^{-1} at 25 °C (United States Salinity Laboratory Staff, 1954); pH was measured using a pH electrode (Orion 9157BNMD). Gypsum was quantified using thermogravimetry (Artieda et al., 2006), calcium carbonate equivalent (CCE) was determined by gasometry and organic matter (OM) was quantified by the Walkley-Black method. Particle size distribution (PSD) was determined by a laser diffraction analyser Mastersizer 3000-Hydro LV. To compare the composition of the soil profiles, the proportions of CCE, gypsum and OM were calculated at soil depth intervals of 25 cm following Castañeda et al. (2012). The mean value of each of these soil variables was weighted by the width of the soil horizon.

3.3. Micromorphological analysis

Undisturbed blocks of soil horizons were impregnated with a cold-setting polyester resin, and thin sections (135 mm × 58 mm) were prepared using the Guilloré (1985) and described with a microscope under polarizing conditions following Stoops (2003).

3.4. Wind field modelling

The local wind field around the lake was simulated using the numerical model WindStation (v 4.0.3) (Lopes, 2003). Canyon as a Computational Fluid Dynamics (CFD) solver that solves the Reynolds-averaged Navier-Stokes (RANS) equations with a standard $\kappa - \varepsilon$ turbulence model was used. The model constants were set to standard values for atmospheric flows ($C_\mu = 0.033, \sigma_k = 1.0, \sigma_\varepsilon = 1.3$, $C_1 = 1.44$, $C_2 = 1.92$), following Launder and Spalding (1974). These parameters have been extensively validated in the literature for flows over complex topography (e.g., Lopes, 2003) and were considered as appropriate for the semi-arid, neutrally stratified conditions prevailing in the Ebro Basin. The simulation domain covered an area of 4.4 km^2 (2500 × 1760 m) centred on the main lake, and the model inputs included the topography, the surface roughness and the wind conditions. The boundary conditions consisted of:

1. Inlet: A fully developed wind profile following the logarithmic law, with a reference height of 10 m and roughness lengths (z_0) derived from Corine Land Cover maps (ranging from 0.01 m for water bodies to 0.05 m for shrubland). The Corine Land Cover (2018) dataset categories were converted to Manning's roughness coefficients (n) following established literature values (scale 1:100000, Sánchez and Lastra, 2011).
2. Outlet and Top: Open boundaries with zero-gradient conditions for velocity and turbulence quantities to avoid artificial flow compression.
3. Ground: A non-slip condition with wall functions to account for surface roughness effects on the near-surface velocity gradient.

Two scenarios were simulated for the wind conditions, based on available records from 2004 to 2024 from Híjar and Caspe weather stations, with a wind direction and representative speed (Fig. 2). We applied the software default values, based on Counihan's (1975), for the boundary layer profiles in terms of turbulence intensity and dissipation length scale. The statistical computation of the wind was performed at a height of 10 m above ground level.

3.5. OSL dating

Optically Stimulated Luminescence (OSL) dating was applied to estimate the chronology of CHI1 and CHI2 deposit profiles. A total of 4 samples were collected, one from CHI1 and three from CHI2 at different depths from three sand layers in stratigraphic order. Samples were collected using opaque tubes inserted horizontally into the level of interest and the surrounding matrix was also sampled to measure the moisture content and the radionuclide concentration. All procedures, including physical-chemical treatment for quartz grains extraction, OSL measurements, burial dose estimation, dose rate calculation and analysis for age determination have been carried out at the luminescence laboratory of the National Centre for Research on Human Evolution (CENIEH). Quartz grains of sizes 180–250 μm were extracted from the samples, under controlled light conditions using standard procedures. Once in the darkroom, the sediment from the first 3 cm of each side of the tubes was discarded and only the central part, never exposed to sunlight since deposition, was used for luminescence measurements. The standard procedures applied on this un-exposed material involved chemical treatment with hydrochloric acid and hydrogen peroxide to remove carbonates and organic matter respectively, density separation to keep the quartz-rich fraction with density between 2.62 and 2.7 gcm^{-2} and a 40% hydrofluoric acid treatment for 45 min. This last step would dissolve feldspar grains if present, and remove the outer layer of the quartz grains, affected by alpha radiation. Ages were calculated with the relation

$$\text{Age (ka)} = \text{burial dose (Gy)}/\text{dose rate (Gy/Ka)}$$

where *ky* is kilo years and *Gy* is the unit of radiation dose, gray. The burial dose is estimated from the luminescence response of quartz grains and the dose rate is the dose received per kiloyear based on the concentration of radionuclides present in the matrix (Medialdea and Rivera-Silva, 2022).

Luminescence measurements were carried out in a Risø TL/OSL DA-20 luminescence reader, following the SAR protocol (Single-Aliquot Regenerative-Dose; Murray and Wintle, 2000, 2003). The preheat temperature for the measurement sequences was assigned according to the results of a dose recovery test carried out on artificially bleached aliquots, beta irradiated with ~200 Gy. Three aliquots were measured at each temperature ranging from 200 to 260 °C, and a cutheat 20 °C lower. The best response was observed for a preheat temperature of 240 °C and a cutheat of 220 °C (Fig. S1). The OSL of 24–48 quartz multi-grain aliquots of 2 mm diameter from each sample were measured in order to obtain representative dose distributions. This aliquot size has been preferred as it provides enough resolution on doses to detect the effect of incomplete bleaching. A bigger aliquot size would contain too many grains, so due to an averaging effect this is avoided by reducing the number of grains per aliquot. The resulting dose populations have been reduced by removing the outliers, identified as those values outside 1.5 times the interquartile range, which were excluded from the burial dose calculation. The derived dose populations were normally distributed with overdispersion values ≤30%. Therefore, the Central Age Model (CAM; Galbraith et al., 1999) has been considered appropriate to estimate the burial dose (Arnold and Roberts, 2009).

Dose rates to an infinite matrix were calculated from the contribution of beta, gamma and cosmic radiation. Beta and gamma contributions were based on the concentration of uranium, thorium, potassium and rubidium measured by ICP mass spectrometry at Intertek (Table S in Supplementary Material). The cosmic contribution was determined based on the burial depth and density of sedimentary material, latitude, longitude and altitude (Prescott and Hutton, 1994). In the total dose rate, the attenuation caused by moisture and grain size was taken into account. The present water content was considered as the minimum possible at the time of burial. The present moisture plus 5% with an added error of 5% to account for variability during the burial time was considered as representative (Table S).

3.6. Data analysis

Statistical analyses among soil variables were performed with R Commander (Fox, 2005). We used Spearman's correlation analysis to study the relation between carbonates (CCE) and gypsum content. We

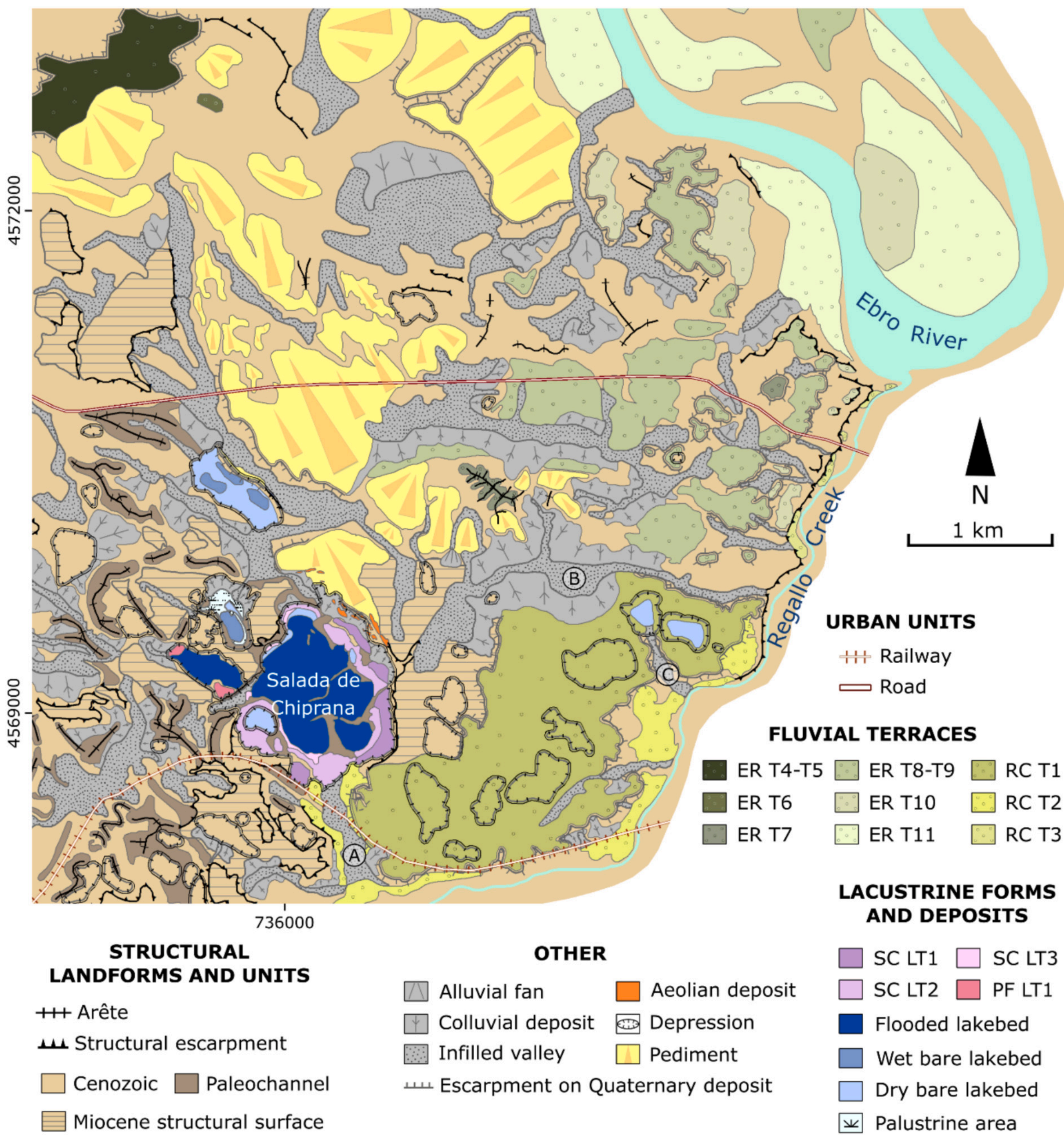

Fig. 3. Detailed geomorphologic map of the study area, Chiprana lacustrine basin and its relationship with the River Ebro and Regallo Creek terraces. A, B, C: Infilled paleovalleys cited in the text. In the legend: ER: River Ebro; RC: Regallo Creek; SC: Salada de Chiprana.

applied multiple linear regressions to explain the variability in the concentration of carbonates or gypsum using as explanatory variables the soil profile studied, the sampling depth, and the various particle size classes. Only variables with a *P*-value of less than 0.05 were retained in the model. Models were checked for the main statistical assumptions.

4. Results

4.1. Main landforms and deposits

The detailed geomorphological map of the study area (Fig. 3) includes landforms of different origin, i.e. structural, fluvial and lacustrine, and illustrates the main context of the wetland complex and especially its relationship to the River Ebro deposits. Morphologically the lacustrine complex is located in a transition zone between two contrasting sectors. The western sector is represented by a hilly area (Figs. 1c and 3) with a certain relief roughness linked to structural landforms on Miocene sandstones, like stepped platforms and paleochannels on horizontal sandstones, and closed depressions excavated among them.

In contrast, the central-eastern sector has low-relief (Fig. 1c), with abundant Quaternary fluvial deposits, gentle slopes and many closed depressions (Fig. 3). It is constituted by a number of fluvial terraces of the River Ebro and Regallo Creek. Several pediments connect all these levels and are composed of thin deposits of silts, sands and gravels. Up to 8 terrace levels have been identified for the River Ebro, and 3 for the Regallo Creek. Their absolute and relative heights, and statistical deviations appear in Table 1. The River Ebro terraces are formed by typical channel facies deposits, several meters thick, with clast-supported polymictic gravels including quartzites and granitic rocks, most of them of Pyrenean provenance. The high-level ER T7 forms an isolated hill from which several pediments expand radially. This residual hill is surrounded by terrace ER T8–9 (Fig. 3), which forms a wide palaeomeander. The remaining terraces are distributed to the east until the present River Ebro channel, whose valley is dammed at this point (Mequinenza Reservoir).

The Regallo Creek, incised on the alluvial plain of the River Ebro, forms a straight valley 5 km long, running SW-NE. From the three terrace levels identified in this creek, the oldest one is also the most extensive, forming a very gentle ramp with morphological characteristics transitional between a pure terrace surface and a pediment. Terrace T2 also has high altitudinal variability and expands along a perched flat-bottomed N-S oriented valley which connects Chiprana lacustrine basin with Regallo Valley (point A in Fig. 3). The deposits of the River Regallo terraces are much thinner than those of the River Ebro, always less than 2 m, and are composed by finer components, usually subangular calcareous clasts in a cross-laminated medium-coarse sandy matrix.

Table 1
Selected metrics of the lacustrine (LT) and fluvial (T) terraces as obtained from LiDAR data. Relative heights are measured with respect to the present average river shores (Ebro and Regallo fluvial channels), or to the average water level in the Chiprana and Prado del Farol lakes. SD: standard deviation.

Location	Terrace	Elevation (m a.s.l.)				Relative height
		Max	Median	Min	SD	
River Ebro	T4-T5	249.3	221.8	180.2	16.7	91–133
	T6	210.1	196.0	184.6	4.7	72–98
	T7	187.5	175.3	150.0	7.8	38–75
	T8-T9	169.5	148.2	115.2	7.5	26–47
	T10	150.8	130.5	112.7	5.1	12–24
	T11 Present channel	133.6	119.0 112.0	112.4	3.7	0–4
Regallo Creek	T1	159.9	150.0	125.3	6.1	13–30
	T2	156.9	138.8	121.4	7.9	6–10
	T3	125.6	116.9	113.5	2.6	0–5
Salada de Chiprana	LT1	152.7	144.6	141.0	2.0	7–10
	LT2	147.3	141.9	139.3	1.3	3–6
	LT3	144.8	139.3	137.2	0.9	1–3
Prado del Farol	LT1	148.4	143.5	141.3	1.3	2–4

Regarding the nature of lakes in the study zone, although closed depressions appear on different morphological units, like fluvial terraces or structural platforms, most of the lakes are located at the foot of the western sector dominated by morphostructural platforms. Their morphology is usually controlled by the disposition and geometry of surrounding paleochannels and escarpments. Fig. 3 includes a distinction among permanently flooded lakebeds, intermittent lake bottoms (wet bare lakebeds), and dry bare lakebeds. Palustrine areas surrounding some lakes have been also represented.

Fig. 4 shows the detailed geomorphology map of the Chiprana endorheic system. Chiprana Lake exhibits a permanently flooded bed and occupies the bottom of a depression of 75 ha delimited by an escarpment which encloses three lacustrine terraces (Table 1 and Figs. 3 and 4). The lake shore is strongly controlled by sandstone paleochannels (brown in Fig. 4), some of them generating compartments of the water body during low water levels. The NW border of the lake is limited by a vertical escarpment of about 12 m. To the NW of Chiprana Lake, Prado del Farol (Fig. 4), appears as a 7.3 ha basin NW-SE elongated and completely flooded, while Salada de las Roces, with 8.6 ha has a vegetated rim enclosing a central dry bare bottom.

A group of scattered small aeolian deposits arranged in small, several metre long, parallel ridges, have been identified along the NE side of Chiprana depression, between 143 m and 151 m a.s.l. (Fig. 4). They are located upon a general gentle slope angle of 4° towards the lake and present a limited vertical development, in general less than 2 m. Some of these deposits are not represented at the scale of the map due to their small dimensions. Soil profile CHI2 was excavated and studied in one of these deposits (see Fig. 4 for location).

Apart from the main lake depressions described above, other shallow and dry depressions appear on the fluvial terraces and between paleochannels. They present different directions of elongation and most of them exhibit shallow dish and funnel shapes (Figs. 3 and 4). Only the lowest ones show evidence of occasional bottom flooding (blue bottom in Fig. 3). Flat-bottomed valleys are ubiquitous, especially in the central-eastern sector. Many of them are diffluent and perched with respect to the main fluvial valleys, without any clear trace of current functionality. They present straight lateral borders with topographic knicks and microescarpments, suggesting collapse processes. Some of these valleys, indicated by capital letters in Fig. 3, stand out by their morphology: (A) South of Chiprana, with N-S direction connecting Chiprana with Regallo Creek valley, (B) East of Chiprana with *E*-W direction, in the contact between terraces of the Ebro and Regallo courses, gently draining towards Chiprana Lake, and (C) a short valley connecting a closed depression to the Regallo valley. These valleys do not correspond to any drainage basin but connect depressions and exhibit lateral escarpments similar to those produced by settlements of the substratum.

Height distribution of Quaternary deposits of the zone is showed and statistically analysed in Fig. 5. The River Ebro shows a nearly constant drop between consecutive levels, except for the most recent ones, which mark a certain decrease in the vertical incision trend. Regallo Creek shows the opposite trend: an increase in the incision rate during the generation of the most recent terrace level. Lacustrine terraces of the Chiprana Lake are stepped, maintaining a constant vertical drop between levels. Finally, Prado del Farol lake terrace develops at an intermediate height between the two highest levels of Chiprana Lake. According to this distribution, the highest lacustrine level of Chiprana is inset in the T1 level of Regallo and in T8-T9 level of Ebro.

4.2. Main characteristics of the soils

The two soil profiles studied in Chiprana allow us to characterize the lower lacustrine terrace LT3 formed by fine detrital materials (profile CHI1), and the aeolian deposits located on the NE edge of the depression

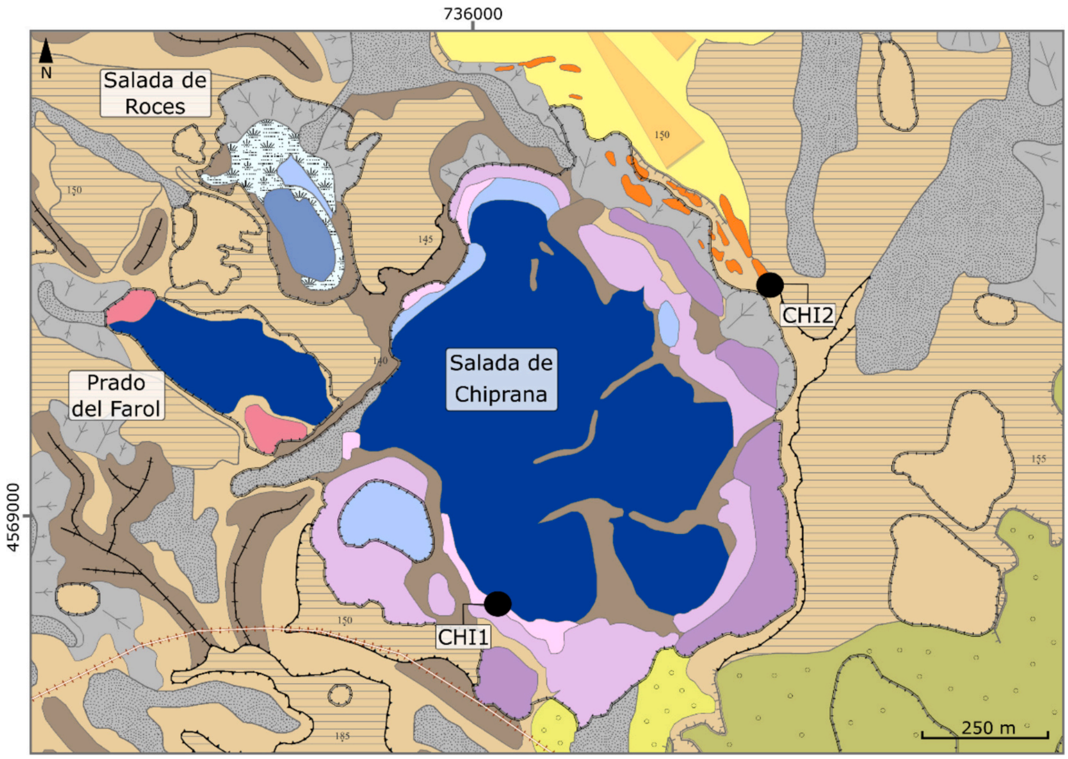

Fig. 4. Detailed geomorphological map of the Chiprana lacustrine basin (Salada de Chiprana complex), showing the location of soil profiles studied (black circles), CHI1 in the lacustrine terrace LT3 and CHI2 in the aeolian deposits. Legend is the same as in Fig. 3.

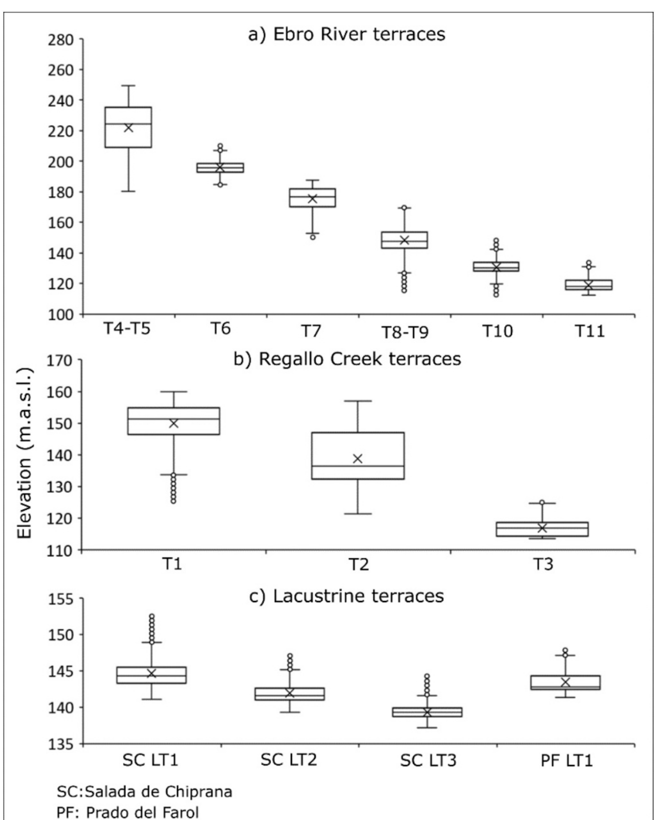

Fig. 5. Elevation distribution of the terraces in the River Ebro (a), Regallo Creek (b), and Chiprana and Prado del Farol basins (c), based on the LiDAR DEM data. Interquartile range box, median and its confidence interval, and outliers are represented.

(profile CHI2) (Fig. 6a and b). The soil moisture regime was xeric for the terrace and aridic for the aeolian deposit. The temperature regime was thermic for both. Soils were classified as Gypsic Haploxerept (CHI1) and Xeric Haplogypsid (CHI2) (Soil Survey Staff (SSS), 2022) and the diagnostic horizons were Ochric for epipedons and Gypsic for almost all the subsurface horizons.

The terrace soil, CHI1, showed a sequence of horizons A-B-C under a thin (2 cm) and loose organic horizon. The A horizon presented a fine to very fine texture and very strong granular structure, favoured by the high density of the vegetation cover, mainly *Suaeda vera* and *Limonium* sp. No saline crust was observed in CHI1. The soil structure of CHI1 weakened with depth, from strong granular to weak subangular blocky, with a smooth transition to a C horizon with massive structure. The persistent morphological features throughout the soil profile were the i) common to very frequent vermicular gypsum accumulations associated with root channels and pores, ii) few to common reduction and oxidation mottles (masses) indicating episodes of water saturation in the soil, and iii) common tubular porosity due to worm activity (Fig. 7).

The soil profile CHI2 developed in a talus with 30% slope covered by halonitrophilous vegetation (*Salsola vermiculata*, *S. kali*, *Heliotropium europaeum*, *Stipa* sp., *Plantago* sp.). The sequence of horizons was A-C and a series of different C horizons were identified based on noticeable lithological discontinuities (Fig. 6d), many of them with slightly wavy boundaries (Fig. 7). A noticeable planar cross lamination can be observed, with sedimentary sets dipping about 28–30° lakewards, as indicated with arrows in Fig. 6d. Apart from the surface horizon which presented a weak subangular blocky structure, the rest of the pedon was characterized by a persistent weakly developed platy structure whose size varied from very fine to coarse. In general, the soil showed a moderate to strong compaction with carbonates and gypsum accumulations. Soft powdery carbonate accumulations occurred in all horizons at a depth of between 57 cm and 112 cm. Other types of soft accumulations included frequent fine vermiform gypsum, gypsum nodules and gypsum concentrations associated with the faces of the bands, mostly in the same C horizons with carbonate accumulations. In general, CHI2

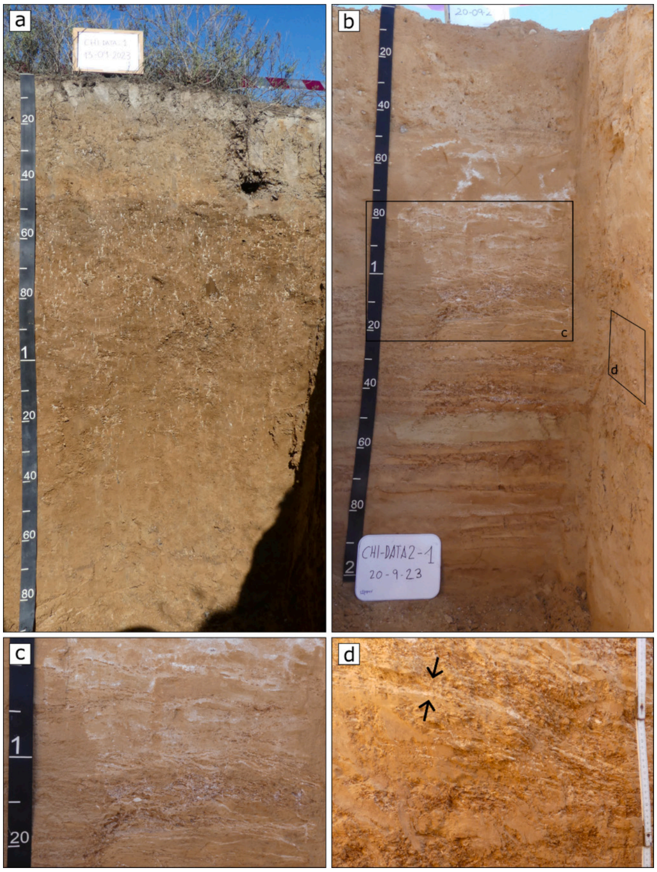

Fig. 6. The soil profiles sampled, CHI1 (a) and CHI2 (b). Vermicular gypsum accumulations are visible in CHI1 and gypsum accumulations aligned along sedimentary sets in CHI2 (c). In the lateral side of CHI2 (d) the sedimentary sets dipping lakeward are indicated with arrows; note the interbedded gypsum layers.

showed much more abrupt transitions between horizons than CHI1 and included a remarkable irregular boundary at 107/112 cm (Figs. 6d and 7) and subvertical infilled cracks in 6C and 9C horizons, at depths of 107–126 cm and 139–153 cm, respectively. Some bands showed gentle undulations also observable at microscopic scale together with evidence of clay translocation, limpid clay coating fragments and silt intercalations. Sedimentary sets of the aeolian deposit with a mean inclination of 28° lakewards appeared at a depth of 120 cm (Fig. 9e).

Soil pH ranged from 7.6 to 8.8 (Table 2) being slightly higher in CHI1 than in CHI2. Soil salinity is an outstanding feature of CHI1, with ECe values varying from 6.1 to 30.1 dS m^{-1}. In contrast, the salinity in the CHI2 horizons reached a maximum ECe of 10.8 dS m^{-1} at a depth of 45/47–52 cm. Deeper horizons were non saline, though with some slightly saline horizons interbedded.

Soils were rich in calcium carbonate (CCE), with a mean concentration of 39.4% (range = 25.4–48%). CHI1 showed a slight increase in CEE with depth (Table 2). Regarding the vertical distribution of CCE in CHI2, there were three different sequences of horizons separated by two horizons (7C and 12C) with a relatively small amount of CCE. In the first sequence, CCE increased with a depth of up to 120 cm, then it remained stable from 140 to 170 cm, and afterwards decreased with a depth from 190 to 305 cm (Table 2). In contrast, the range of soil gypsum content was higher, from less than 5% to 51% (Table 2) and there was a strong negative correlation between gypsum and CCE content ($r = -0.84$; $P < 0.001$). Gypsum content was very low throughout CHI1 (less than 10% at depths of more than 10 cm). In CHI2 gypsum content was less than 10% in horizons below 110 cm except for two spikes at depths of around 130–140 cm and 170 cm, where it reached 22% and 15%, respectively.

The mean organic matter (OM) content of mineral horizons was 0.4% (range = 0.2–2.4%), and 1.2% for A horizons. The content in the organic horizon of CHI1 was 9.7% (Table 2). As expected, OM content decreased with depth in CHI1, while the CHI2 pedon showed a more complex vertical pattern of OM content, with decreasing and increasing sequences and randomly distributed variations even to the end of the surveyed depth. Two notable relative OM content increments appeared down in the CHI2 profile, reaching 1.2% and 1% OM at depths of around 130–140 cm and 170 cm, respectively, coinciding with the horizons with a higher relative content of gypsum.

The predominant USDA textural class is loam for the two soils, and sandy loam in the upper half of CHI2 pedon. In CHI1, the sand content increases with depth, with a fine surface horizon, Agy, free of sand, 55% of silt and 45% of clay (Table 2). Further down in this profile, the Cgy4 horizon, at a depth of 135–180 cm, showed the highest content of sand-sized particles, 83%. CHI2 showed a high textural variability with soil depth, with alternating increases and decreases of sand or silt-sized particles (Table 2).

None of the studied variables influenced the CCE content. But the gypsum content varied between the two soil profiles ($P = 0.02$), CHI2 showing higher values than CHI1, and according to the sample depth ($P = 0.02$), with a general decrease with increasing depth. But studying the two profiles separately, sampling depth had no explanatory power in either of the profiles. In CHI1, the gypsum content was positively related to the coarse sand fraction and negatively related to the fine sand fraction, following:

$$\text{Gypsum} = 12\text{x}8 \text{ coarse sand} - 0.2 \text{ fine sand} \quad R^2 = 0.89; P = 0.005$$

while for the CHI2 profile the gypsum content was explained by the medium sand fraction:

$$\text{Gypsum} = 4 + 2 \text{ medium sand} \quad R^2 = 0.58; P = 0.001$$

The mean value of the sum of CCE plus gypsum content in the two profiles was 55%, and reached 77% in CHI2. Comparing the vertical distribution of the sum of gypsum plus CCE at equal intervals of 25 cm, it remained constant throughout the CHI1. But it decreased in CHI2 down to 225 cm and increased from 225 cm onwards, mainly because of the gypsum content variability with depth (Fig. 8a and b).

Micromorphological observations of CHI1 show a mixture of micritic carbonate plus siliciclastic groundmass, with a granular microstructure in the upper horizon and a predominant weakly subangular blocky microstructure in the subsurface horizons. The main components in the upper horizon (0–10 cm) are vegetal remains with Fe hypocoatings and oribatid excrements, abundant millimetric channels with lenticular gypsum crystals infillings. In the intermediate horizon (55–60 cm) no gypsum is observed (Fig. 9a). The abundant fauna activity developed a high circular and elongated porosity and coalescent excrements. Main components are the high proportion of quartz grains with ostracod shell fragments, degraded clay remains and Fe—Mn pore coatings. In the lower part of the pedon (from 135 cm) the high bioporosity can be empty or infilled with gypsum crystals and quartz grains, with subsequent fauna activity building new porosity in the previous infillings. Despite this intense reworking of the material, patches of the original laminated sediment are preserved together with ferruginized root remains triggered from non-aerated reducing soil conditions (Fig. 9b).

The adjacent surface soil crust in CHI1 (Fig. 9c and d) provided additional information about the surface soil conditions in the transitional situation between the terrace (dry) and the lake (flooded). Under the salt efflorescence (mainly with bloedite and thenardite, as identified in the soil thin section), the microbial mats formed under flooding conditions are degraded when exposed, losing their laminar organization. Intertwined micrometric layers (thickness ~ 500 μm) of lenticular gypsum and fragmented microbial mats are mixed with microcrystalline carbonate micromass (<1 μm of crystal size). Unlike the surface horizon formed under aerial conditions and cover of vegetation, the frequent

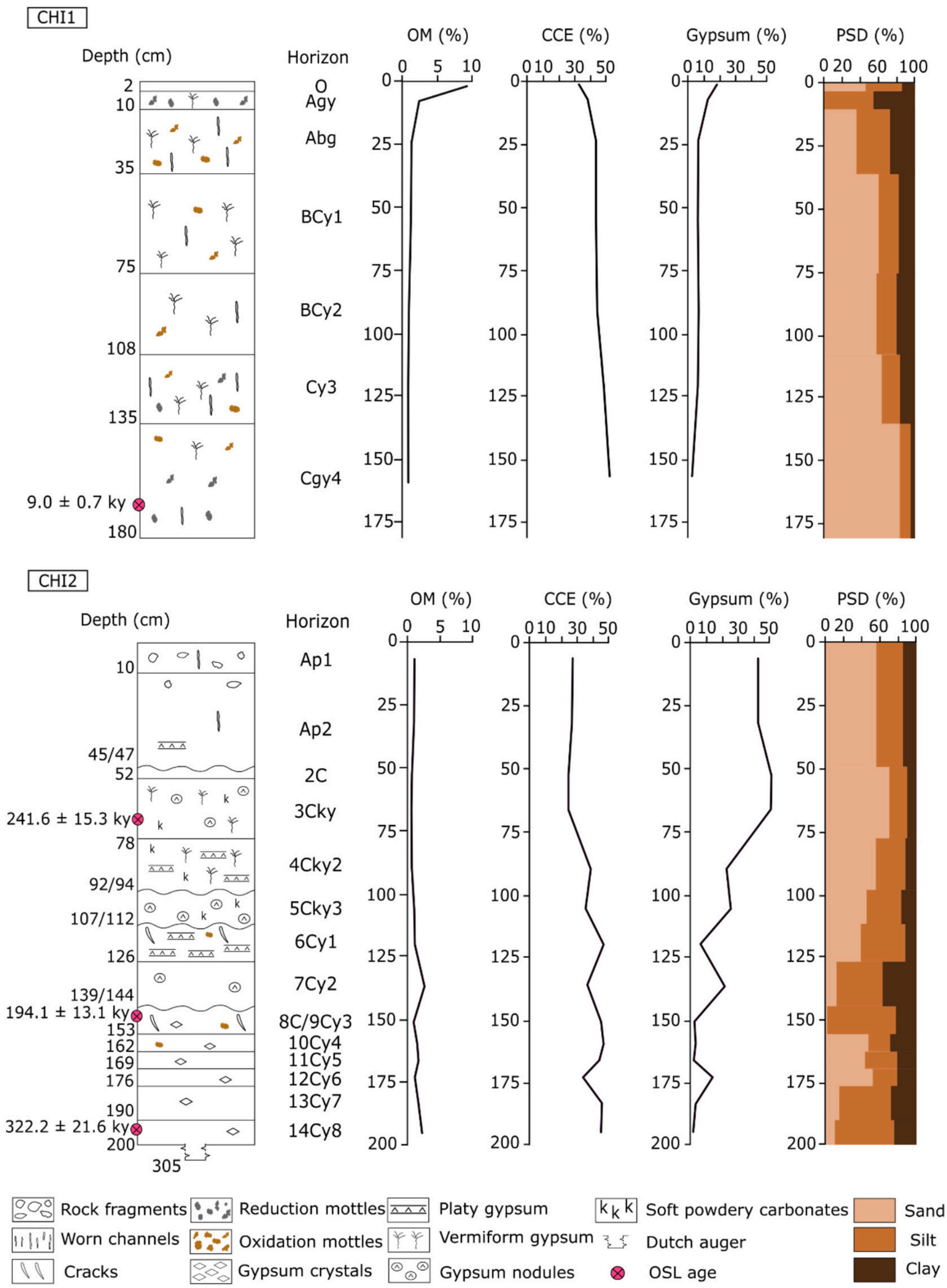

Fig. 7. Summary of the main morphological and compositional features of the two studied soil profiles. Samples for dating are also indicated, as red dots. OM: organic matter; CCE: calcium carbonate equivalent; PSD: particle size distribution. (For interpretation of the references to colour in this figure legend, the reader is referred to the web version of this article.)

root remains of the crust are not affected by oribatid excrements. Under the degraded mat, the accumulation of lenticular gypsum crystals increases to 60% in volume (Fig. 9d), with a more homogenous crystal size, and the pores frequently present Fe hypocoatings probably inherited from non-aerated conditions.

CHI2 shows a granular microstructure with local laminar structure. The main components are the abundant subangular coarse quartz fragments (100–400 μm) and the lenticular gypsum crystals (190–220 μm) frequently broken showing cleavage planes, corroded borders, internal dissolution and replacement by micritic carbonates. Several families of gypsum crystals, from very fine incipient imperfect crystals to well-developed lenticular gypsum, and gypsum crystals growing inside previous gypsum crystals. Microcrystalline carbonates appear around the gypsum fragments and also along the cleavage planes, promoting inside and outside crystal decay followed by gypsum recrystallizations as small lenses. In the upper horizons, there are degraded root remains with oribatid excrements. The channels are coated with gypsum crystals and plant remains, which also appear aligned following the sedimentary

Table 2
Physical and chemical properties of the two soils studied at Chiprana. See Fig. 4 for pedon location. EC1:5: electrical conductivity of the 1:5 soil:water extract; ECe: electrical conductivity of the saturated extract; CCE: calcium carbonate equivalent; OM: organic matter.

Horizon	Depth	EC 1:5	ECe	pH 1:5	CCE	Gypsum	OM	Sand	Silt	Clay
	cm	dS m^{-1} at 25 °C		%						
	Pedon CHI1									
O	0–2	3.1	6.1	7.7	31.8	17.5	9.7	45.9	39.4	14.7
Agy[1]	2-10	3.9	12.2	7.7	36.7	13.0	2.4	0.0	54.5	45.5
Abg	10-35	5.7	25.3	8.4	40.8	6.9	1.4	35.7	36.6	27.7
BCy1[2]	35–75	6.6	30.1	8.8	39.6	6.9	1.0	59.8	22.2	18.0
BCy2[2]	75–108	6.5	27.4	8.2	40.4	7.9	0.9	57.3	22.2	20.5
Cy3[2]	108–135	4.7	18.3	8.5	46.8	7.0	0.9	63.4	19.9	16.7
Cgy4[2]	135–180	3.6	17.3	8.2	47.7	<3%	0.4	83.2	11.1	5.7
	Pedon CHI2									
Ap1[3]	0–10	2.6	5.8	7.6	28.8	43.4	0.6	57.8	28.0	14.2
Ap2[3]	10–45/47									
2C	45/47–52	2.9	10.8	7.7	25.4	51.4	0.2	68.3	20.9	7.4
3Cky[2]	52–78									
4Cky2[2]	78–92/94	2.9	8.7	7.8	39.3	22.2	0.4	56.1	33.9	10.0
5Cky3[2]	92/94–107/112	3.1	9.3	7.8	36.0	26.6	0.7	43.8	40.0	16.3
6Cy1[2]	107/112–126	2.8	6.9	7.8	47.5	6.7	0.6	38.0	48.2	13.8
7Cy2[2]	126–139/144	2.9	5.7	7.8	38.6	21.8	1.2	12.0	51.2	36.8
8C/9Cy3[2]	139/144–153	1.9	6.3	7.8	45.4	<3%	0.3	1.7	77.5	20.7
10Cy4[2]	153–162	2.5	5.8	7.8	47.0	4.0	0.8	44.0	36.4	19.6
11Cy5[2]	162–169	1.7	5.4	7.8	44.9	<3%	1.0	42.1	37.6	20.3
12Cy6[2]	169–176	2.7	6.8	7.8	36.5	15.2	0.4	50.0	29.3	20.7
13Cy7[2]	176–190	2.8	7.3	7.7	46.6	4.8	0.8	16.3	56.1	27.6
14Cy8[2]	190–200	2.3	4.9	7.7	45.9	3.2	0.4	9.5	65.4	25.1
	200–220	2.1	5.8	7.8	43.6	<3%	0.6	20.4	39.0	40.6
	220–240	1.5	–	8.0	44.0	<3%	0.4	58.5	17.9	23.6
	240–260	2.6	5.5	7.9	41.0	8.3	0.7	35.0	35.7	29.3
	260–280	2.6	5.3	7.8	36.8	18.5	0.5	49.0	32.9	18.1
	280–295	2.5	5.0	7.8	37.0	17.3	0.3	56.2	25.5	18.3
	295–305	2.5	–	7.8	32.4	27.0	0.7	52.0	22.5	25.5

[1] Ochric-Gypsic; [2]Gypsic; [3]Ochric.

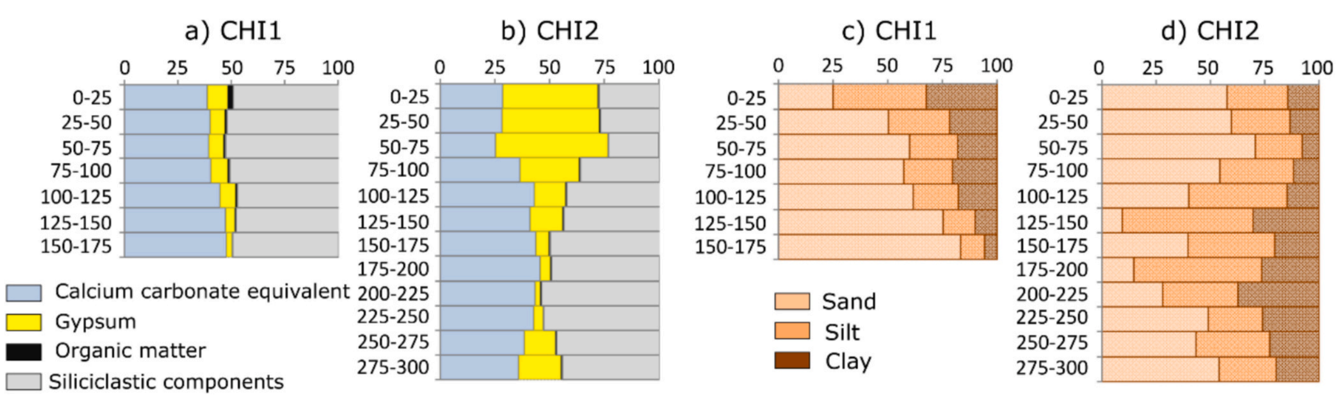

Fig. 8. Sliced soil profiles showing the vertical distribution of the soil composition (percentage of calcium carbonate, gypsum, organic matter and siliciclastic components) in CHI1 (a) and CHI2 (b), and the particle size distribution in CHI1 (c) and CHI2 (d). Slices were calculated for the 25 cm thick synthetic soil layers.

lamination.

In the upper and intermediate horizons, centimeter *en-échelon* brittle structures with an apparent dipping of about 45° are visible on laminated siliciclastic material with poor sorting (Fig. 9e), probably resulting from the mechanical action of transport and deposition along the slope. In agreement with the macromorphological observations of the lateral walls of the pit, microsedimentary laminations are identified, like cross laminations with an apparent dipping of about 30–40° lakewards, with asymmetrical ripple profiles and reactivation surfaces (Fig. 9f).

In deep horizons (below 135 cm) there is an increase in sorted sediments translocation through the groundmass, mainly clay illuviation and silt to fine sand intercalations together with clay laminae fragments and layered clay plus gypsum coatings. We observed clay and silty clay coatings, gypsum infillings, and self-fragmentation and relocation of the groundmass with sand infilling. The root porosity is frequent, with the pores aligned following planes of sedimentary weakness. This self – reorganization of the soil includes sorted and homogeneous infillings and frequent collapse structures probably as a result of structural instability (Fig. 9g).

Other edaphic processes include decarbonation by root activity and associated esparite grains (queras) up to 140 cm deep in the profile, manganese accumulations as dendritic masses or as dense pore coatings. Frequent faunal passage features comprise lumbricid channels sometimes with crescent infillings. Down in the profile, the bioturbation increases the porosity favouring the lenticular gypsum crystals growing in bands. A crushing of the groundmass is observed together with the opening of strongly accommodated planar voids probably due to the well-known pressure produced by the growth of lenticular gypsum (Fig. 9h).

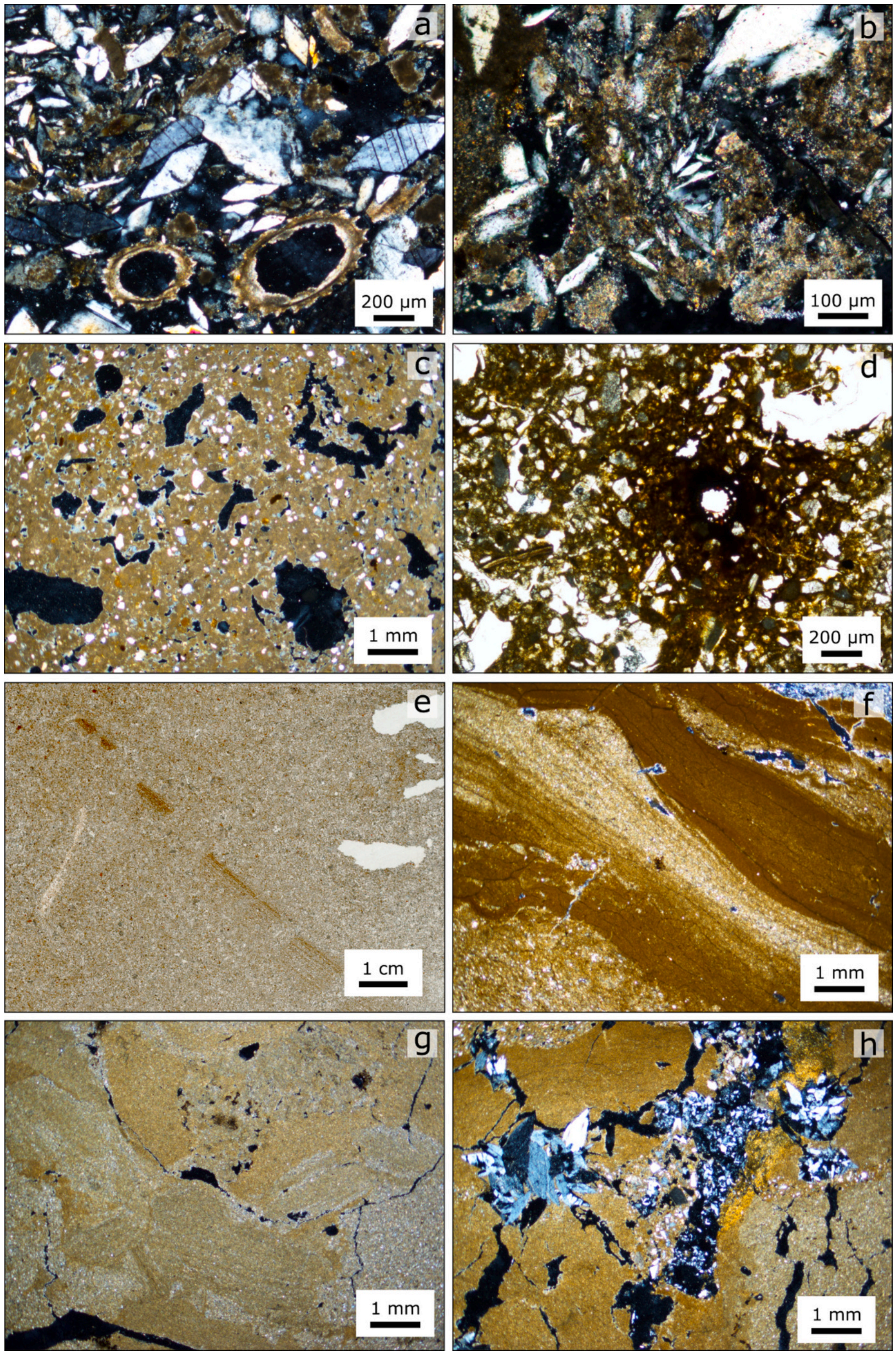

Fig. 9. Micromorphotographs of Chiprana soils showing: a) lenticular gypsum crystals of the soil crust with cleavage planes intergrowing with plant and oogonia remains of CHI1 (O, 0–10); b) gypsum infillings and crystals of CHI1 affected by corrosion under the algal mats (O, 0–10); c) abundant unfilled faunal channels in the carbonate-rich groundmass of CHI1 subsurface horizon (BCy1, 55–60); d) Fe hypocoating of preserved root remains of CHI1 lower horizon (Cgy4, 135–150); e) incipient fragmented laminae on fine material with apparent inclination of 45° lakewards in CHI2 (2C, 45/47–52); f) sedimentary cross laminations and asymmetrical ripple profiles with reactivation surfaces in CHI2 (5Cky3, 92–105); g) collapse structure showing the original material in the walls and the groundmass fragments of a different sized gravity fallen material (7Cy2, 126–139/144); h) different families of lenticular gypsum crystals growing in and opening the accommodated planar voids, and coatings of clay, silt, and clay mixed with silt (7Cy2, 126–139/144).

4.3. Grain size distribution in CHI2

Fig. 10a presents the grain size distribution of samples taken in the CHI2 profile (see Fig. 7 for location of the samples within the profile). The analysis was made by using a bi-log frequency scale, following the method of Visher (1969), in order to distinguish the different grain-sized populations. According to this method, the distribution curve is fragmented in a number of segments, where the truncation points between segments can be interpreted as the point separating different grain populations due to the different mechanism of sediment transport: traction, saltation and suspension. Each population can also be divided into other minor sub-populations, as a function of the different intensities that the transport agent can achieve during the sediment transportation and sedimentation.

The resulting curves show a variety of patterns indicating the complexity of processes responsible for their generation. The traction

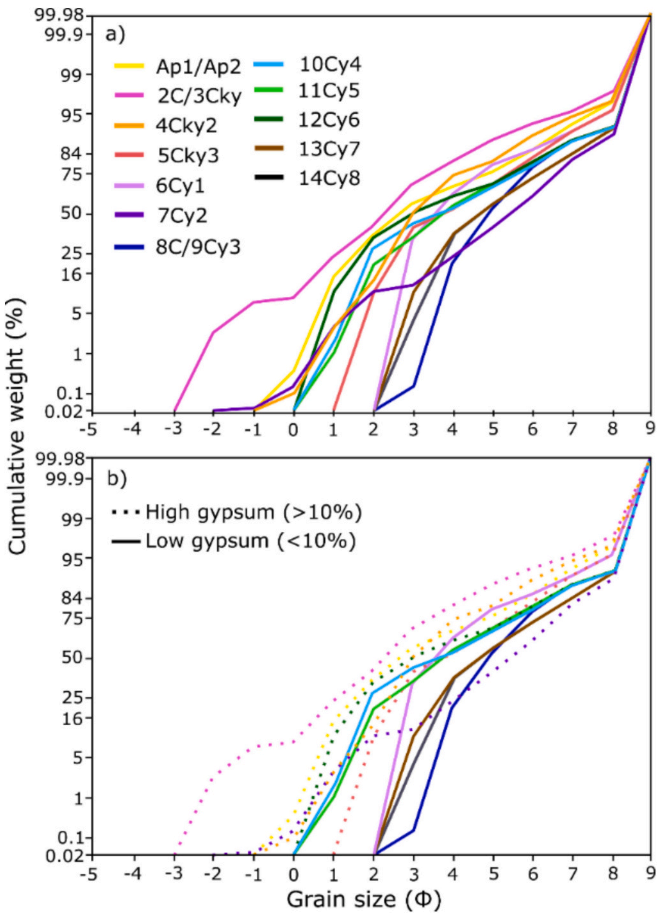

Fig. 10. Granulometric curve of CHI2 horizons following Visher (1969), (a) and differentiated by the high/low gypsum content (b) (10% as threshold).

population, associated with grain sizes lower than 0 Φ, is virtually absent in the curves. The saltation population represents a significant fraction of the deposits, especially in the 0–4 Φ grain size interval. The suspension population (Φ > 4) is the most important one in most curves, concurrent with the fine-grained materials of CHI2, between coarse clay and fine sand. However, in this case care must be taken with the possible role of gypsum in the transport, deposition and edaphic processes (Fig. 10b).

Samples with a high content in gypsum, typical of the surface soil horizons (Ap1/Ap2), show a higher grain size and a clear traction-creep population together with an important suspension population. Deeper horizons present an intermediate grain size between sand and silt, and do not exhibit any traction population, regardless of the gypsum proportion (5Cky3 and 12Cy6 have a high gypsum content; 6Cy1, 10Cy4, 11Cy5, 13Cy7, and 14Cy8 have a low gypsum content). Only 8C/9Cy3, a silty horizon with low gypsum content, presents a clear division among traction, two-saltation and one suspension populations, with a bi-log distribution quite similar to the pattern proposed by Visher (1969) for dune sediments. The higher proportion of suspension population in this sample may be related to its silty size.

4.4. Effects of predominant winds over Chiprana area

The flow vectors of Fig. 11 show the direction in which sedimentary material can be mobilised and then deposited. The spatial heterogeneity of the wind and the recognition of wind patterns which could be responsible for the presence of the aeolian sediments depend on the predominant wind direction applied to the model. In the case of small lakes like this, non-uniform wind patterns can occur due to sheltering from the surrounding topography. However, the regional NW wind direction results in a mostly uniform wind field over the entire simulated area (Fig. 11a) and no interaction with the local topography is observed. These winds are parallel to the longitudinal development of the aeolian deposits. Conversely, the model for westerly winds shows significant interaction with the local orography (Fig. 11b). The simulation predicts distinct zones of wind speed attenuation and flow separation on the leeward (eastern) side of small topographic highs, coinciding with the mapped aeolian deposit.

The model resulting from the westerly winds predominant at the Caspe weather station (Fig. 2) seem to be more sensitive to the orography of the lake surroundings (Fig. 11b). The wind field has a mean wind speed of 4.5 ms^{-1} ($\pm$ 2.1 ms^{-1}), i.e. weak breeze, and a range from 0.1 to 11 ms^{-1} (strong breeze) in the Chiprana area. Local zones of wind speed attenuation with dispersion of the main wind direction are generated around the lake, mostly associated with topography around the lake and the upward forms such as the NE slopes. Besides, small wind shadow areas are generated over the water's surface in the lee side of the exposed paleochannels whereas the W wind flow remains consistent (though attenuated) through two main W-E corridors.

Regarding uncertainty and sensitivity of the wind model applied in this work, the primary source of uncertainty is the input wind direction and topographic resolution. By simulating the two dominant wind components (NW and W) and using a high-resolution LiDAR DEM (5 m), we addressed the most critical variables. The spatial consistency between the simulated deceleration zones and the present location of the paleosols (field evidence) serves as a robust "ground-truth" validation of the model's predictive capability.

4.5. Quartz OSL ages obtained on Chiprana soils

The dose distributions obtained for the four samples (Fig. S2) have overdispersion values between 25 and 30% (Table 3), similar to those observed on dose recovery experiments, where the aliquots measured were artificially bleached and irradiated. This suggests that the studied units are not significantly affected by extrinsic factors like incomplete bleaching or post-depositional disturbance. Table 3 summarizes the absolute ages obtained from the two profiles, CHI1 and CHI2. They represent the age of the sediment deposition in very distant time periods, 9.0 (±0.7) ka at the bottom of the lower terrace (CHI1, LT3), and between 202.7 (± 11.1) and 322.2 ka (± 21.6) in the aeolian CHI2 profile (CHI2–1 to CHI2–3). The incredibly old CHI2 dating is consistent along the sequence of three horizons, at 195, 145 and 65 cm depth. The estimated ages for the two uppermost samples CHI2–1 (225.8 ± 12.9 ka) and CHI2–2 (202.7 ± 11.1 ka) are consistent with each other within 1-sigma, showing that the OSL technique cannot provide enough resolution to tell the depositional ages of these two units apart.

5. Discussion

5.1. Considerations on the nature of the Chiprana aeolian deposits

The aeolian interpretation of the CHI2 deposits is based both on geomorphological, sedimentological and micromorphological data. Diagnostic aspects of aeolian deposits can be consulted in Glennie (1970), regarding morphology, grain size and internal structure and lamination. In the case of Chiprana Lake, five characteristics support the aeolian nature of this deposit: height above the lake, arrangement and geometry, morphology, internal structure and grain size. Regarding height of appearance, they are located between 8 and 13 m above the present lake's level, on gentle slopes with no signs of any past lacustrine flooding or fluvial influence. The arrangement and geometry of the deposits consist in a set of elongated bodies parallel to the NW wind direction. Their morphology resembles that of climbing dunes associated with winds blowing up slopes or obstacles with inclinations not higher than 55° (Dłużewski et al., 2023). They develop a windward side,

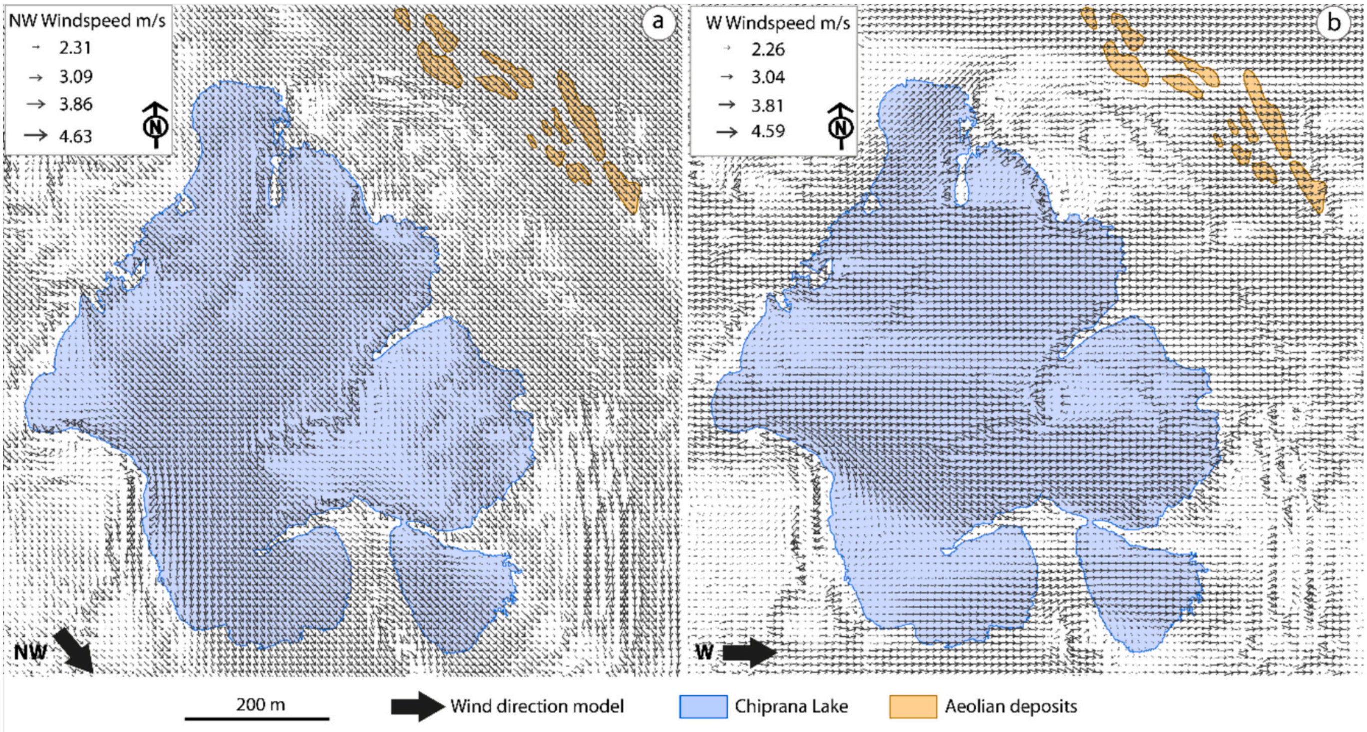

Fig. 11. Wind flows field over Chiprana Lake area shown over the LiDAR DEM data, resulting from the wind scenarios of Híjar-NW (a) and Caspe-W (b) weather stations (Wind roses in Fig. 2).

Table 3
OSL dating information; this includes dose rate calculated from radionuclide concentration, burial doses estimated from the OSL response of quartz and derived age for each of the four samples. Ages are reported with 1-sigma associated error. Samples are identified with both, the field and laboratory codes.

Sample	Laboratory code	Dose rate (Gy/ka)			Burial dose (Gy)			OD (%)	Age (ka)		
CHI1	LM23297–4	1.87	±	0.07	16.8	±	1.1	30	9.0	±	0.7
CHI2–1	LM23297–5	1.95	±	0.07	440.2	±	19.1	28	225.8	±	12.9
CHI2–2	LM23297–6	2.08	±	0.08	422.5	±	16.7	25	202.7	±	11.1
CHI2–3	LM23297–7	1.19	±	0.05	383.2	±	20.8	25	322.2	±	21.6

parallel to the underlying slope, a crest and a downwind slip face. The sediments studied in the CHI2 profile are located on the lakewards slope, that represents the windward side of the aeolian deposit. The internal structure of climbing dunes has rarely been studied, although Rodríguez-Santalla et al. (2025) recently published a synthesis of the sedimentology and internal geometrical characteristics of a climbing dune in SW Spain. The windward face is characterized by inclined laminae, broadly parallel to the slope of the underlying ground, typically between 30° and 35° like those observed in the lateral walls of the CHI2 profile. Small ripple migration structures associated with local truncations and variations at different scales, like those observed in Fig. 9f, reflect disruptions of the deposition process (Fu et al., 2019). Regarding possible slope processes in the genesis of CHI2 deposit, in this case upslope sources are exclusively formed by medium to coarse sands and gravels of fluvial origin, that could not justify the prevailing grain size of the studied accumulations and discard any possible sedimentary supply from upper points in the slope.

Regarding grain size, at the scale of the outcrop, the CHI2 deposit is marked by dominant fine materials. However, the grain size curves obtained in the present study (Fig. 10), after comparison with reference curves proposed by Visher (1969), let us conclude the prevalence of sediment transport by suspension and the absence of traction transport. The only geomorphic process able to develop this kind of selective transport mode in the zone is wind. However, we must recognize that granulometric curves are complex, relatively common in ancient deposits, and difficult to interpret. The grain transportation may have been affected by the aggregation tendency of clay and gypsum due to electrostatic forces (Casby-Horton et al., 2015). Moreover, the grain size distribution (Fig. 10a) can reflect edaphic processes, especially due to gypsum reworking. Additionally, the use of laser diffraction or other water-based procedures to determine the particle size distribution in gypsum-rich soils can produce artefacts following gypsum dissolution (Casby-Horton et al., 2015). This error in textural characterisation can be more significant than the possible error in gypsum quantification due to the release of water from possible clay or hydrated minerals when using thermogravimetry (Álvarez et al., 2022).

The NW predominant wind in the River Ebro valley (Ortega et al., 2022) was likely the regional prevalent wind direction during the Quaternary (Plata et al., 2021; Poch et al., 2021). In the case of Chiprana Basin, the lake is located in a sheltered area with respect to the NW dominant winds, especially the deepest part of the lakebed (Guerrero et al., 1991; Valero-Garcés et al., 2000). The NW-wind simulation (Fig. 11a) hardly justifies the location of the studied aeolian deposits, given the orientation and dip of the laminae recognized in profile CHI2 (Fig. 9e), though the set of aeolian deposits (Fig. 4) does elongate in a NW direction. In contrast, the W-wind simulation (Fig. 11b) generates a wind velocity gradient in the gentle lee side of the basin and low velocity areas in the location of the aeolian deposits. This suggests a direct geomorphic link: westerly winds, though perhaps less frequent or intense than the NW wind, would have been highly effective at promoting sediment deposition in these specific, topographically sheltered locations. This provides a robust physical mechanism for the formation of the perched aeolian deposit upon which the palaeosol developed, highlighting the divergence between regional transport (NW winds) and local depositional patterns (W winds). It must be recognized that model results are sensitive to input parameters like surface roughness. Similarly, the simulation assumes the modern-day topography, which may differ from the Middle Pleistocene landscape. However, the macro-scale topographic features controlling the flow, such as the *E*-W valley orientation, are structurally controlled and likely persisted to present, making the simulation a valid first-order approximation of palaeowind patterns.

The occurrence of plate-shaped gypsum fragments and gypsum crystals with broken edges, similar to those described in nearby areas by Mees et al. (2012) indicates a detrital origin, and the presence of euhedral crystals suggests transport at short distances. The material must have come from the bottom of the basin due to the occurrence of intermittent flooding and drought episodes related to a fluctuating Chiprana Lake. The evaporitic sediments should have been removed by saltation processes. The fragmented microlaminae morphologies (Fig. 9e) of the sedimentary sets can be related to the mechanical traction through the slope during the aeolian deposition. Subsequent edaphic processes such as the faunal activity (Fig. 9h), translocation of the groundmass due to structural instability (Fig. 9g), reworking of the gypsum in pores by crystal growing and dissolution, and carbonation and decarbonation processes locally favoured by plant root activity are common with other aeolian deposits (Álvarez et al., 2024).

The successive lithological discontinuities of CHI2, some of them erosive (Fig. 7), can be associated with aeolian deflation processes between periods of sediment accretion. The vegetal remains arranged parallel to the aeolian laminae suggest the presence of vegetation cover that could have acted as sediment trap retaining these aeolian sediments, as in the *nebkha* dune type. The alternance of horizons with distinct gypsum content (Table 2) indicates a complex history with periods of sediment accretion in the absence of a gypsum source, and periods of stability suggested by the relative increase in organic matter content in 7Cy2 and 11Cy5 horizons (Table 2). The preservation of the original laminar structure (Tierra et al., 2024) in most horizons over such a long period (more than 300 ka) suggests a limited pedogenesis. Gypsum accumulations aligned with sedimentary sets (Figs. 6c and d) may have acted as a cementation agent due to the strong electrostatic adhesion of lenticular gypsum favouring the preservation of the structure. Besides the detrital gypsum crystals, the occurrence of size-families of gypsum lentils filling pores, indicates different pedogenic phases.

Aeolian deposits linked to lakes in semiarid areas have been documented in the Ebro Basin (Sánchez-Navarro et al., 1998; Gutiérrez et al., 2005, 2013; Luzón et al., 2012; Boixadera et al., 2015; Plata et al., 2019, 2021) and over the world (Torgersen, 1984; Magee, 1991; Timms, 1992; Liu et al., 2011). However, aeolian deposits of silts and clays are very unusual in Spain, and virtually absent in the rest of Europe. In the center of the Iberian Peninsula, occupying some low-relief areas in the region of La Mancha, Bernat Rebollal and Pérez-González (2008) described a number of Quaternary dunes rich in silts and clays. Unlike siliciclastic aeolian materials, the aeolian deposit CHI2 of Chiprana is formed by gypsum plus carbonates up to 76%, as occur in other locations of the Ebro Basin (Mees et al., 2012).

5.2. A conceptual model of the genesis and evolution of the Chiprana endorheic basin

Unlike the abundant studies on dating and correlation of terrace levels of the River Ebro and its tributaries on the left River Ebro bank (Sancho et al., 2016; Parés et al., 2021), there is a significant scarcity of studies addressing the correspondence among the right margin tributaries. The highest Chiprana lacustrine terrace is inset about 6 m on the T8-T9 terrace level of the River Ebro and some 5.5 m on the T1 terrace level of the Regallo Creek (Fig. 3 and Table 1). Terrace T8 (+26–47 m) corresponds to a palaeomeander (Fig. 12a) already mentioned by previous authors (Quirantes, 1969; Ibáñez, 1976; Mensua and Ibáñez, 1977; Julián, 1990; Solà et al., 1997). Fuller et al. (1996) dated to 253 ka (+ 72, −67) a river terrace of the same relative height (+ 30–34 m) in the nearby River Guadalope, a tributary of the River Ebro located next to the East. The dating results from CHI2, between 225.8 (± 12.9) and 322.2 (± 21.6) ka broadly agree with this old terrace of the River Guadalope. Terrace level T8 was deposited during the Middle Pleistocene, in correspondence to the Penultimate Glacial Period, Riss. The Chiprana Lake depression should have developed once the alluvial plain (T8) was formed, and therefore the depression must be chronologically younger - otherwise the sedimentation of the rivers Ebro and Regallo would have infilled the depression. On the other hand, Regallo terrace T1 forms a complex pediment-terrace surface inset in the River Ebro terrace T8-T9 and extends to the SE and E (Fig. 12b) ending at a height of about +13 m.

Regarding the origin of the initial Chiprana depression, the karstification process is discarded because of the siliciclastic substratum (Cuevas et al., 2010). Aeolian processes could have generated some subtle depressions or gentle blowouts, during the Upper Pleistocene. The CHI2 sediments probably correspond to these initial moments. Once the initial depression formed in the contact between the sandstone hills and the alluvial plain, preferential water flows would have concentrated.

Some closed depressions in this endorheic complex show infilled, flat-bottomed paleovalleys with abrupt lateral borders connected to Regallo Creek (A, B, C in Fig. 3). In this sense, Jódar et al. (2020) identified preferential shallow subsurface water flows after geoelectrical resistivity profiles through flat-bottomed valleys around Chiprana Lake, including valley B in Fig. 3. This is consistent evidence of the activity of piping processes in the area. On the other hand, micromorphological observations of CHI2 pedon show micro collapses and translocations of silt and clay (Fig. 9g), and clay coatings (Fig. 9h). Sodium content favouring the materials' instability have been previously reported in soils of the Chiprana Basin (Cuchí, 1986). These data suggest piping as a process was involved in the development of the lacustrine system through a slow, small-scale and non-superficial evolution on the landscape scale.

Piping processes are very common in the Ebro Basin (Gutiérrez et al., 1997; Desir and Marín, 2007), in some cases producing diffuse leaking out of water (Desir et al., 2018). The forms observed in Chiprana Lake resemble those of other similar depressions formed by bottom collapse due to piping processes (Wright Jr., 1964; Shaw and Bryant, 2011; Castañeda et al., 2017). It is very likely that the individuation and incision of Regallo Creek increased the local hydraulic gradient, triggering piping processes and lacustrine basin subsidence (Fig. 12c). A straight flat-bottomed valley with abrupt borders connected the early Chiprana lacustrine basin with the Regallo Valley. This valley should start in Terrace T1 (+13 m) (Fig. 12b), in correspondence with the Guadalope terraces +11 and + 20 m, with ages ranging between 26.4 and 53.4 ka (Fuller et al., 1996), in correspondence with the onset of the Last Glacial Period, Würm. This valley would finish at a height equivalent to the Regallo terrace level T2. By comparison with the Guadalope River terrace system, the age of this terrace could be estimated at 9–18 ka (Fuller et al., 1996), in correspondence to the beginning of the deglaciation period after the Würm glacial maximum. Finally, the successive incision episodes of the River Ebro might have rejuvenated piping processes and produced renewed collapses or subsidence episodes, presently represented by the dry, flat-bottomed valleys (Fig. 3 and section 4.1) with steep borders that connect Chiprana lacustrine basin and other minor closed depressions to the Regallo Creek valley (Fig. 12d). During this period the Chiprana Basin transformed into a fully lacustrine environment, with the generation of a stepped system of lacustrine terraces (Fig. 4), reflecting different expansion episodes during the early Holocene. The more recent evolution of the lake was inferred from the sedimentological analysis of boreholes by Doyle et al. (2022a), from a pre-1800 a.C. permanent saline lake with local gypsum

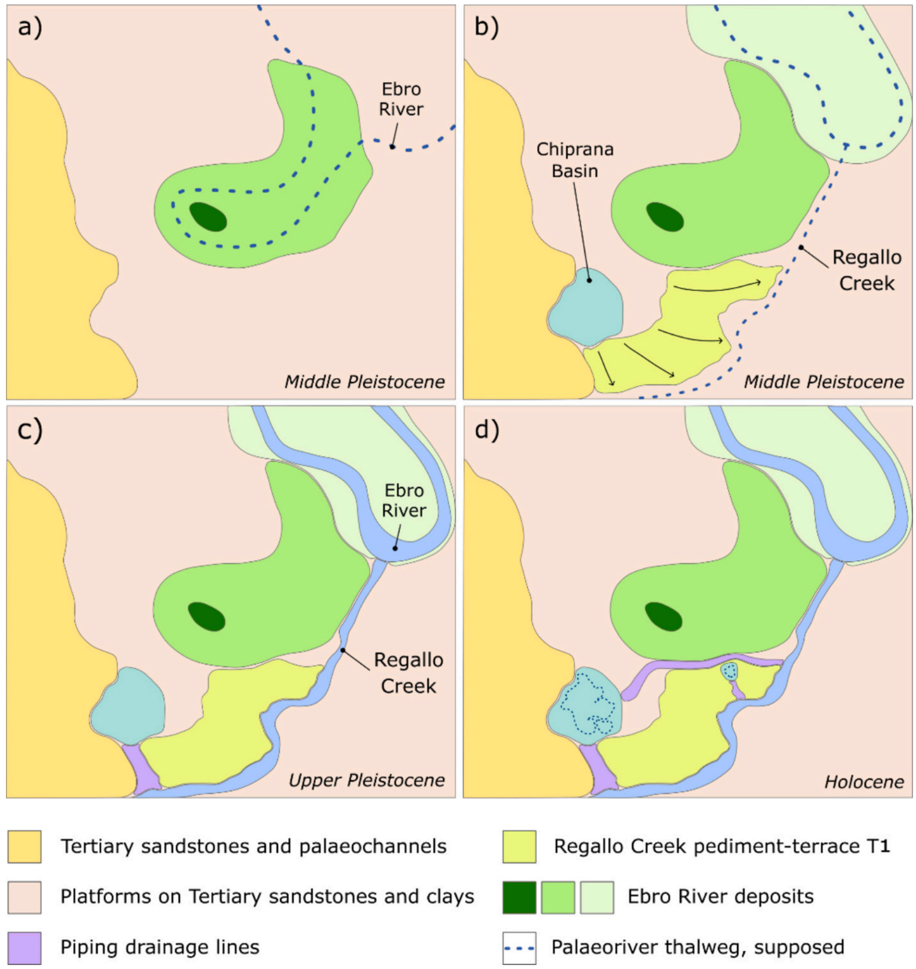

Fig. 12. Proposed stages of evolution of the Chiprana Basin with development of: a) the River Ebro meander; b) meander capture and River Ebro incision, setting of the Regallo Creek and T1 level, and a subtle blowout depression; c) piping processes; d) a reactivation of piping processes and subsidence of Chiprana Basin. Chronological ages are estimates.

precipitation and heterolithic silty sediments, to a shallow hypersaline and presently permanent lake with microbial mats and extensive gypsum growth.

5.3. Palaeoclimate considerations

Lacustrine records older than 30–40 ka are very uncommon, and especially those including Middle Pleistocene deposits are exceptional, not only in Southern Europe and the Mediterranean Basin (Roberts and Reed, 2009; Tzedakis, 2009), but also worldwide (Parton et al., 2018). In Spain, a group of wetlands located in the central Iberian Peninsula (Tablas de Daimiel) have provided data about Middle Pleistocene vegetation variability that were used by Valdeolmillos-Rodríguez et al. (2011) to make palaeoclimatic and palaeoenvironmental interpretations. Other significant contribution is the information revealed by palaeomagnetic data at the Atapuerca archaeological site, located in central-northern Spain (Bógalo et al., 2021). In this sense, the Middle Pleistocene aeolian deposits associated with Chiprana Lake represent an outstanding reference for the reconstruction of palaeoclimatic conditions in this part of the Iberian Peninsula and Southern Europe, due to the scarcity of palaeoenvironmental data associated with that period.

The CHI2 aeolian deposit is indicative of different palaeoenvironments and water level fluctuations in Chiprana Lake, i.e., climatic variations. The CHI2 dating is exceptional because they characterize one of the oldest aeolian dated deposits within the Quaternary evolution of the Ebro Basin (up to 322 ka). This age broadly coincides with the Riss glaciation during which favourable conditions for aeolization occurred with a cold and dry climate. Taking into account one of the most recent time distributions of the Quaternary climatostratigraphic isotope stages (Railsback et al., 2015; PAGES, Past Interglacials Working Group, 2016; Palacios et al., 2024), sample CHI2–3 (322.2 ka) corresponds to MIS 9e and sample CHI2–1 (225.8 ka) to MIS 7e. These stages, represented by odd numbers, are associated with warm episodes between cold pulses within the Riss glacial period (MIS 10). According to this, terrace level T8 of the River Ebro could have formed during the cold and humid stage MIS 10, while the moment of initial generation of the Chiprana Depression would be younger during stage MIS 9. Dry episodes during warm stages MIS 9 and 7 would have favoured the desiccation of the lake bottom and the generation of the aeolian deposit CHI 2. In central Spain Middle Pleistocene stages MIS 9 and 7 were characterized by the expansion of wooded areas with xerophilous steppe vegetation in lowlands, longer periods of dryness and temperatures probably higher than during the Holocene (Valdeolmillos-Rodríguez et al., 2011; Blain et al., 2012). Between both periods, MIS 8 consisted in a weak glacial stage (Bógalo et al., 2021; Van der Made et al., 2025).

In the Ebro Basin, general aridification during the Middle Pleistocene was already deduced by Luzón et al. (2012), who described aeolian deposits between 99 and 173 ka, while Plata et al. (2019, 2021) dated different loess units with ages ranging from 17 to 34 ka to 100–130 ka. Torres-Guerrero et al. (2023, 2024) dated by OSL a loess deposit in an interval between 150 and 352 ka. In other zones of the Iberian Peninsula Late Pleistocene deposits associated with aridity are also common.

Bernat Rebollal and Pérez-González (2008) dated clay dunes in central Spain from the period 29.5 to 15 ka, corresponding to cold and dry conditions (mainly Heinrich events HE-3 and HE-2 and the Last Glacial Maximum).

The lowest lacustrine terrace (+1 m) was dated to 9.0 ± 0.7 ka, showing sediments clearly associated with lacustrine conditions (CHI1), although under a quite fluctuant hydrological regime. The CHI1 soil can be characterized by a homogeneity evidenced by a relatively continuous lacustrine carbonate sedimentation of the lake. Only the sandy Cgy4 horizon at the pedon bottom (180 cm) shows inherited morphologies related to redox processes and biological activity (Fig. 9d) that indicate temporarily emerged soil conditions with vegetation cover. During this recent historical period Chiprana Lake transformed from a fluctuant semi-arid playa lake to a permanent saline lake, especially after the Medieval Warm Period (Valero-Garcés et al., 2000).

The lacustrine terraces indicate a previous larger extent of the water bodies (Fig. 4), and a later retraction of the water surface, probably due to a general trend to arid conditions. The 9.0 ± 0.7 ka of the Chiprana lacustrine terrace indicates an Early Holocene period of deposition, while the dating of lacustrine sediments accumulated below the present lake bottom gave ages of 5.72 ± 0.6 ka (provided by pollen analysis at 1.8 m depth given by Davis Davis, 1994), and 3.4 ± 0.2 ka (^{14}C age at 1.3 m depth given by Valero-Garcés et al., 2000). Previous palaeoclimatic reconstruction of Chiprana Lake (Davis Davis, 1994; Valero-Garcés et al., 2000; Davis and Stevenson, 2007; González-Sampériz et al., 2009) identified an increase in lake water levels in the Ebro Basin during the Early Holocene caused by colder climates and/or higher precipitation. This humid period would have been replaced by a drier period afterwards. Close to the CHI1 dating, at around 8.2 ka, there was an abrupt change to a colder climate on a global scale (Roffet-Salque et al., 2018). Different authors agree on the change from a humid to a more arid climate in the region around this age, marked by a shift from numerous archaeological settlements to the near absence of archaeological remains (González-Sampériz et al., 2009) and a higher carbon content in the sedimentological records, according to Davis and Stevenson (2007). These authors suggested that this event could have started in the centre of the Ebro Basin up to 600 years earlier. Nevertheless, it is difficult to identify abrupt climatic changes in these types of palaeoenvironment because of the sedimentary discontinuities due to wind erosion (Davis and Stevenson, 2007; González-Sampériz et al., 2008, 2009).

6. Conclusions

The combination of different techniques and disciplines for establishing a conceptual model for the genesis and evolution of the Chiprana lacustrine system is an integrated methodological approach which can be useful also if applied to other environments. The observations at different scales, from landscape to the microscope, provided consistent results. The detailed geomorphological map provided the basic framework to explain the fluvial and lacustrine processes in the basin. The soils associated with the lake deposits, aeolian and lacustrine, are a key source of information to understand the environmental and climatic changes. The old age of the aeolian deposits studied proves that aeolization processes in the Ebro Basin started early, during the penultimate glacial phase, Riss Glaciation, a very poorly understood period on the Iberian Peninsula.

The genesis of the Chiprana lacustrine basin was the result of water and aeolian combination processes, under a fluctuating cold and dry climate in the Middle Pleistocene. Fluvial processes, related to the development of a River Ebro meander and its later abandonment by regional fluvial incision, favoured the generation of a closed depression during the Middle Pleistocene (MIS 9). Piping processes, very active along the Ebro Basin due to the textural and chemical characteristics of many sediments and soils in the region, can be triggered by base level lowering. This process is very rapid, much faster than fluvial erosion, and very likely occurred in the study area as a consequence of the regional fluvial incision. This hypothesis could be applied to the very incipient origin of the Chiprana Basin as well. More aeolian deposits will be needed in order to check the extent and importance of the aeolian processes during this period. Traces of piping processes can be found all the way along the study area, at different scales, such as straight valley-like depressions and trenches, closed depressions with overflow channels, etc., apart from micro and mesoforms observable on soils.

This work contributes to the knowledge of the Quaternary endorheism of the Ebro Basin. The time-lapse identified in the Chiprana Lake between the aeolian processes and the lower lacustrine terrace, dated in the Early Holocene, should be filled with more data from other lakes located in a similar climatic context. In this sense, the evolution of endorheism during the Upper Pleistocene and its relationship with palaeoclimate evolution still needs more data to be assessed satisfactory.

CRediT authorship contribution statement

M. Tierra: Writing – original draft, Visualization, Methodology, Investigation, Conceptualization. **C. Castañeda:** Writing – original draft, Supervision, Project administration, Investigation, Funding acquisition, Conceptualization. **F.J. Gracia:** Writing – original draft, Investigation, Conceptualization. **R. Rodríguez-Ochoa:** Writing – review & editing, Investigation, Conceptualization. **J.R. Olarieta:** Writing – review & editing, Investigation, Formal analysis. **A. Medialdea:** Resources, Investigation. **O. Castillo:** Software, Resources.

Declaration of competing interest

The authors declare that they have no known competing financial interests or personal relationships that could have appeared to influence the work reported in this paper.

Acknowledgement

This work was supported by the grants PID2021-127170OB-I00 funded by MCIN/AEI/10.13039/501100011033 and by "ERDF A way of making Europe", and TED2021-130303B-I00 funded by MCIN/AEI/10.13039/501100011033 and by the "European Union NextGeneration EU/PRTR". This is a contribution to Andalusia Research Group (P.A.I.) RNM 328. The authors would like to thank field work assistant C. Romano and the Nature Protection Agents of the Government of Aragon, soil lab assistants P. Paniagua and E. García, and micromorphology lab assistant F. Acín. We thank the Spanish Agency AEMET for the data from weather stations, and the Scientific and Technique Analysis Services in Pyrenean Institute of Ecology-CSIC in Zaragoza-Jaca (Spain) for their technical support.

Appendix A. Supplementary data

Supplementary data to this article can be found online at https://doi.org/10.1016/j.catena.2026.110058.

Data availability

Soils and geomorphology of "Salada de Chiprana" RAMSAR wetland, NE Spain (Original data) (Mendeley Data)

References

Adams, K.D., 2003. Estimating palaeowind strength from beach deposits. Sedimentology 50, 565–577. https://doi.org/10.1046/j.1365-3091.2003.00565.x.

Álvarez, D., Antúnez, M., Porras, S., Rodríguez-Ochoa, R., Olarieta, J.R., Poch, M., 2022. Quantification of gypsum in soils: methodological proposal. Span. J. Soil Sci. 12, 10669. https://doi.org/10.3389/sjss.2022.10669.

Álvarez, D., Torres-Guerrero, C.A., Travé, A., Preusser, F., Plata, J.M., Poch, R.M., 2024. Queras biogenic carbonates (queras) in loess-palaeosol sequences of the Ebro Basin and their potential use as a palaeoenvironmental proxy. Catena 240, 107969. https://doi.org/10.1016/j.catena.2024.107969.

Anento, J.L., Ponz, A., 1992. Las Saladas de Alcañiz: un complejo estepario a conservar. Cuadernos de Estudios Caspolinos XVIII 247–278.

Arnold, L.J., Roberts, R.G., 2009. Stochastic modelling of multi-grain equivalent dose (D_e) distributions: implications for OSL dating of sediment mixtures. Quat. Geochronol. 4, 204–230. https://doi.org/10.1016/j.quageo.2009.03.003.

Artieda, O., Herrero, J., Drohan, P.J., 2006. A refinement of the differential water loss method for gypsum determination in soils. Soil Sci. Soc. Am. J. 70, 1932–1935. https://doi.org/10.2136/sssaj2006.0043N.

Bernat Rebollal, M., Pérez-González, A., 2008. Inland aeolian deposits of the Iberian Peninsula: sand dunes and clay dunes of the Duero Basin and the Manchega plain. Palaeoclimatic considerations. Geomorphology 102, 207–220. https://doi.org/10.1016/j.geomorph.2008.05.009.

Blain, H.-A., Panera, J., Uribelarrea, D., Rubio-Jara, S., Pérez-González, A., 2012. Characterization of a rapid climate shift at the MIS 8/7 transition in Central Spain (Valdocarros II, autonomous region of Madrid) by means of the herpetological assemblages. Quat. Sci. Rev. 47, 73–81. https://doi.org/10.1016/j.quascirev.2012.05.021.

Bógalo, M.F., Bradák, B., Villalaín, J.J., Calvo-Rathert, M., González, M.I., Heller, F., Ortega, A.I., Parés, J.M., 2021. High-resolution late middle Pleistocene paleoclimatic record from the Galería complex, Atapuerca archaeological site, Spain – an environmental magnetic approach. Quat. Sci. Rev. 251, 106721. https://doi.org/10.1016/j.quascirev.2020.106721.

Casby-Horton, S., Herrero, J., Rolong, N.A., 2015. Chapter four - gypsum soils—their morphology, classification, function, and landscapes. Adv. Agron. 130, 231–290. https://doi.org/10.1016/bs.agron.2014.10.002.

Castañeda, C., García-Vera, M.A., 2008. Water balance in the playa-lakes of an arid environment, Monegros, NE Spain. Hydrogeol. J. 16, 87–102. https://doi.org/10.1007/s10040-007-0230-9.

Castañeda, C., Gracia, F.J., 2017. Recognition and mapping of lacustrine relict coastal features using high resolution aerial photographs and LiDAR data. J. Paleolimnol. 58, 89–99. https://doi.org/10.1007/s10933-017-9956-0.

Castañeda, C., Herrero, J., Casterad, M.A., 2005. Landsat monitoring of playa-lakes in the Spanish Monegros Desert. J. Arid Environ. 63, 497–516. https://doi.org/10.1016/j.jaridenv.2005.03.021.

Castañeda, C., Latorre Garcés, B., Herrero Isern, J., 2012. SLICES (synthetic layers integrating characteristics enclosed in the soil) v. 1.0. Available at: http://hdl.handle.net/10261/60892.

Castañeda, C., Gracia, F.J., Luna, E., Rodríguez-Ochoa, R., 2015. Edaphic and geomorphic evidences of water level fluctuations in the Gallocanta Lake, NE Spain. Geoderma 239-240, 265–279. https://doi.org/10.1016/j.geoderma.2014.11.005.

Castañeda, C., Gracia, F.J., Rodríguez-Ochoa, R., Zarroca, M., Rpqué, C., Linares, R., Decir, G., 2017. Origin and evolution of Sariñena Lake (Central Ebro Basin): a piping-based model. Geomorphology 290, 164–183. https://doi.org/10.1016/j.geomorph.2017.04.013.

Cuevas, J.L., Cabrera, L., Marcuello, A., Arbués, P., Marzo, M., Bellmunt, F., 2010. Exhumed channel sandstone networks within fluvial fan deposits from the oligo-Miocene Caspe formation, south-East Ebro Basin (north-East Spain). Sedimentology 57, 162–189. https://doi.org/10.1111/j.1365-3091.2009.01096.x.

Dantín, J., 1942. Distribución y extensión del endorreísmo aragonés. Estudios Geográficos 8, 505–595.

Davis, B.A.S., 1994. Palaeolimnology and Holocene Environmental Change from Endoreic Lakes in the Ebro Basin, North-East Spain. Newcastle University, p. 319. Available at: http://hdl.handle.net/10443/642.

Davis, B.A.S., Stevenson, A.C., 2007. The 8.2 ka event and the Early–Mid Holocene forest, fires and flooding in the Central Ebro Desert. NE Spain. Quat. Sci. Rev. 26, 1695–1712. https://doi.org/10.1016/j.quascirev.2007.04.007.

De Wit, R., Guerrero, M.C., Legaz, A., Jonkers, H.M., Blocier, L., Gumiaux, C., Gautret, P., 2013. Conservation of a permanent hypersaline lake: management options evaluated from decadal variability of *coleofasciculus chthonoplastes* microbial mats. Aquat. Conserv. Mar. Freshwat. Ecosyst. 23, 532–545. https://insu.hal.science/insu-00771383v1.

Desir, G., Marín, C., 2007. Factors controlling the erosion rates in semi-arid zone (Bardenas Reales, NE Spain). Catena 71, 31–40. https://doi.org/10.1016/j.catena.2006.10.004.

Desir, G., Marín, C., Gracia, F.J., Castañeda, C., Rodríguez, R., Olarieta, J.R., Colino, F., 2018. Los procesos de piping como moduladores del paisaje y la hidrología. In: García, C., Gómez-Pujol, L., Morán-Tejeda, E., Batalla, R.J. (Eds.), Geomorfología del Antropoceno. Universidad de las Islas Baleares, SEG, Palma de Mallorca, Efectos del cambio global sobre los procesos geomorfológicos, pp. 99–102.

Dłużewski, M., Rotnicka, J., Hesp, P., Tomczak, J., 2023. Airflow dynamics and aeolian sand transport across a beach-climbing dune-clifftop dune system. J. Geophys. Res.: Earth Surf. 128. https://doi.org/10.1029/2023JF007316.

Doyle, C., Schröder, S., Corella, J.P., Valero Garcés, B., 2022a. Facies variability and depositional settings of Laguna Salada de Chiprana, and Iberian hypersaline lake. Sedimentology 69, 2615–2641. https://doi.org/10.1111/sed.13005.

Doyle, C., Corella, J.P., Schröder, S., Strauss, H., Bishop, T., Yarwood, J., Valero-Garcés, B., 2022b. Spatio-temporal variations in the geochemistry of Laguna Salada de Chiprana. NE Spain. Geosciences 12 (10), 381. https://doi.org/10.3390/geosciences12100381.

Fox, J., 2005. The R commander: a basic-statistics graphical user Interface to R. J. Stat. Softw. 14 (9), 1–42. https://doi.org/10.18637/jss.v014.i09.

Fu, T., Wu, Y., Tan, L., Li, D., Wen, Y., 2019. Imaging the structure and reconstructing the development of a barchan dune using ground-penetrating radar. Geomorphology 341, 192–202. https://doi.org/10.1016/j.geomorph.2019.05.014.

Fuller, I.C., Macklin, M.G., Passmore, D.G., Brewer, P.A., Lewin, J., Wintle, A.G., 1996. Geochronologies and environmental records of quaternary fluvial sequences in the Guadalope basin, Northeast Spain, based on luminescence dating. In: Branson, J., Brown, A.G., Gregory, K.J. (Eds.), Global Continental Changes: The Context of Palaeohydrology, vol. 115, pp. 99–120. Geol. Soc. Spec. Publ.

Galbraith, R.F., Roberts, R.G., Laslett, G.M., Yoshida, H., Olley, J.M., 1999. Optical dating of single and multiple grains of quartz from Jinmium rock shelter, northern Australia: part 1, experimental design and statistical models. Archaeometry 41, 339–364. https://doi.org/10.1111/j.1475-4754.1999.tb00987.x.

Glennie, K.W., 1970. Desert sedimentary environments. Developments in Sedimentology, 14. Elsevier, Amsterdam, p. 222.

González-Sampériz, P., Valero-Garcés, B.L., Moreno, A., Morellón, M., Navas, A., Machín, J., Delgado-Huertas, A., 2008. Vegetation changes and hydrological fluctuations in the Central Ebro Basin (NE Spain) since the Lateglacial: saline lake records. Palaeogeogr. Palaeoclimatol. Palaeoecol. 259, 157–181. https://doi.org/10.1016/j.palaeo.2007.10.005.

González-Sampériz, P., Utrilla, P., Mazo, C., Valero-Garcés, B., Sopena, M.C., Morellón, M., Sebastián, M., Moreno, A., Martínez-Bea, M., 2009. Patterns of human occupation during the early Holocene in the Central Ebro Basin (NE Spain) in response to the 8.2 ka climatic event. Quat. Res. 71, 121–122. https://doi.org/10.1016/j.yqres.2008.10.006.

Gracia, F.J., Morales, J.A., Castañeda, C., Plomaritis, T., 2021. Shallow lacustrine versus open coastal clastic deposits: morphosedimentary diagnostic indicators and interpretation. Sediment. Geol. 423, 105981. https://doi.org/10.1016/j.sedgeo.2021.105981.

Gracia, F.J., Castañeda, C., Simarro, G., Calvete, D., 2023. Water level control on coastal landform distribution and associated processes in a highly fluctuating shallow lake (Gallocanta Lake, NE Spain). Earth Surf. Process. Landf. 49, 770–786. https://doi.org/10.1002/esp.5735.

Guerrero, M.C., Balsa, J., Pascual, M., Martínez, B., Montes, C., 1991. Caracterización limnológica de la laguna salada de Chiprana (Zaragoza, España) y sus comunidades de bacterias fototróficas. Limnetica 7, 83–96. Available at: http://hdl.handle.net/10486/13678.

Guilloré, P., 1985. Méthode de fabrication mécanique et en série des lames minces, 3. Institut National Agronomique, Paris-Grignon (In French).

Gutiérrez, F., Gutiérrez, M., 2014. Playa-Lakes and yardangs in the Bujaraloz-Sástago endorheic area, Central Ebro Basin. In: Gutiérrez, F., Gutiérrez, M. (Eds.), Landscapes and Landforms of Spain. Springer, Dordrecht, pp. 145–153. https://doi.org/10.1007/978-94-017-8628-7_12.

Gutiérrez, M., Peña, J.L., 1993. Geomorphology and geology of the Ebro depression. In: Gutiérrez, M., Sancho, C., Benito, G. (Eds.), Second Intensive Course on Applied Geomorphology: Arid Regions. University of Zaragoza-Erasmus, pp. 33–88.

Gutiérrez, M., Sancho, C., Benito, G., Sirvent, J., Desir, G., 1997. Quantitative study of piping processes in badland areas of the Ebro Basin, NE Spain. Geomorphology 20, 237–253. https://doi.org/10.1016/S0169-555X(97)00026-3.

Gutiérrez, M., Desir, G., Gutiérrez, F., Sánchez, J.A., Castañeda, C., Lucha, P., 2005. Aeolian Landforms and Saline Lakes (Central Ebro Basin). Field Trip Guide B7, Sixth International Conference on Geomorphology. I.A.G, Zaragoza, Sapin, p. 47.

Gutiérrez, F., Valero-Garcés, B., Desir, G., González-Sampériz, P., Gutiérrez, M., Linares, R., Zarroca, M., Moreno, A., Guerrero, J., Roqué, C., Arnold, L.J., Demuro, M., 2013. Late Holocene evolution of playa lakes in the Central Ebro depression based on geophysical surveys and morpho-stratigraphic analysis of lacustrine terraces. Geomorphology 196, 177–197. https://doi.org/10.1016/j.geomorph.2012.02.013.

Hage, S., Hubert-Ferrari, A., Lamair, L., Avsar, U., El Quahabi, M., Van Daele, M., Boulvain, F., Bahri, M.A., Seret, A., Plenevaux, A., 2017. Flow dynamics at the origin of thin clayey sand lacustrine turbidites: examples from Lake Hazar, Turkey. Sedimentology 64, 1929–1956. https://doi.org/10.1111/sed.12380.

Hare, J.L., Ferguson, J.F., Aiken, C.L.V., Oldow, J.S., 2001. Quantitative characterization and elevation estimation of Lake Lahontan shoreline terraces from high-resolution digital elevation models. J. Geophys. Res. 106, 26761–26774. https://doi.org/10.1029/2001JB000344.

Ibáñez, M.J., 1973. Contribución al estudio del endorreísmo de la depresión del Ebro: el foco endorreico al W. y SW. de Alcañiz (Teruel). Geographica 15, 21–32. https://www.proquest.com/docview/1309719467?sourcetype=Scholarly%20Journals.

Ibáñez, M.J., 1975. El endorreísmo del sector central de la depresión del Ebro. Cuad. de Investig.: Geogr. e Hist. 1, 35–48. Available at: https://publicaciones.unirioja.es/ojs/index.php/cigh/article/view/2439/2308.

Ibáñez, M.J., 1976. El piedemonte ibérico bajo-aragonés. Estudio geomorfológico, CSIC, Instituto de Geografía Aplicada, 523. Patronato "Alonso de Herrera", mapas, Madrid, Spain, p. 12.

Jódar, J., Rubio, F.M., Custodio, E., Martos-Rosillo, S., Pey, J., Herrera, C., Turu, V., Pérez-Bielsa, C., Ibarra, P., Lambán, L.J., 2020. Hydrogeochemical isotopic and geophysical characterization of saline lake systems in semiarid regions: the Salada de Chiprana Lake. Northeastern Spain. Sci. Total Environ. 728, 138848. https://doi.org/10.1016/j.scitotenv.2020.138848.

Liu, D., Abuduwaili, J., Lei, J., Wu, G., Gui, D., 2011. Wind erosion of saline playa sediments and its ecological effects in Ebinur Lake, Xinjiang. China. Environ. Earth Sci. 63, 241–250. https://doi.org/10.1007/s12665-010-0690-4.

Lopes, A.M.G., 2003. WindStation - a software for the simulation of atmospheric flows over complex topography. Environ. Model Softw. 18, 81–96. https://doi.org/10.1016/S1364-8152(02)00024-5.

Luna, E., Castañeda, C., Gracia, F.J., Rodríguez, R., 2016. Late quaternary pedogenesis of lacustrine terraces in Gallocanta Lake, NE Spain. Catena 147, 372–385. https://doi.org/10.1016/j.catena.2016.07.046.

Luzón, A., Rodríguez-López, J.P., Pérez, A., Soriano, M.A., Gil, H., Pocoví, A., 2012. Karst subsidence as a control on the accumulation and preservation of aeolian deposits: a Pleistocene example from a proglacial outwash setting, Ebro Basin, Spain. Sedimentology 59, 2199–2225. https://doi.org/10.1111/j.1365-3091.2012.01341.x.

Magee, J.W., 1991. Late quaternary lacustrine, groundwater, aeolian and pedogenic gypsum in the Prungle Lakes, southeastern Australia. Palaeogeogr. Palaeoclimatol. Palaeoecol. 84, 3–42. https://doi.org/10.1016/0031-0182(91)90033-N.

MAPA, 1994. Métodos oficiales de análisis. Tomo III. Ministerio de Agricultura, Pesca y Alimentación, Madrid, pp. 115–117.

Martín-Puertas, C., Jiménez-Espejo, F., Martínez-Ruiz, F., Nieto-Moreno, V., Rodrigo, M., Mata, M.P., Valero-Garcés, B.L., 2010. Late Holocene climate variability in the southwestern Mediterranean region: an integrated marine and terrestrial geochemical approach. Clim. Past 6, 807–816. https://doi.org/10.5194/cp-6-807-2010.

May, J.H., May, S.M., Marx, S.K., Cohen, T.J., Schuster, M., Sims, A., 2022. Towards understanding desert shorelines—coastal landforms and dynamics around ephemeral Lake Eyre north, South Australia. Trans. R. Soc. S. Aust. 146 (1), 59–89. https://doi.org/10.1080/03721426.2022.2050506.

McFadden, L.D., Wells, S.G., Brown, W.J., Enzell, Y., 1992. Soil genesis on beach ridges of pluvial Lake Mojave: implications for Holocene lacustrine and eolian events in the Mojave Desert, Southern California. Catena 19, 77–97. https://doi.org/10.1016/0341-8162(92)90018-7.

McGlue, M.M., Cohen, A.S., Ellis, G.S., Kowler, A.L., 2013. Late quaternary stratigraphy, sedimentology and geochemistry of an underfilled lake basin in the Puna plateau (Northwest Argentina). Basin Res. 25, 638–658. https://doi.org/10.1111/bre.12025.

Medialdea, A., Rivera-Silva, J., 2022. Datación por luminiscencia: ópticamente estimulada (OSL) y termoluminiscencia (TL). Cuaternario y Geomorfología 36, 3–4. https://doi.org/10.17735/cyg.v36i3-4.96428.

Mees, F., Castañeda, C., Herrero, J., van Ranst, E., 2012. The nature and significance of variations in gypsum crystal morphology in dry lake basins. J. Sediment. Res. 82, 37–52. https://doi.org/10.2110/jsr.2012.3.

Mensua, S., Ibáñez, M.J., 1977. Terrazas y glacis del centro de la Depresión del Ebro. Universidad de Zaragoza, Reunión Nacional del Grupo de Trabajo del Cuaternario, p. 18.

Mermut, A.R., Acton, D.F., 1984. The age of some Holocene soils on the ear Lake terraces in Saskkatchewan. Can. J. Soil Sci. 64, 163–172. https://doi.org/10.4141/cjss84-018.

Moreno, A., González-Sampériz, P., Morellón, M., Valero-Garcés, B., Fletcher, W.J., 2012. Northern Iberian abrupt climate dynamics during the last glacial cycle: a view from lacustrine sediments. Quat. Sci. Rev. 36, 139–153. https://doi.org/10.1016/j.quascirev.2010.06.031.

Murray, A.S., Wintle, A.G., 2000. Luminescence dating of quartz using an improved single-aliquot regenerative-dose protocol. Radiat. Meas. 32, 57–73. https://doi.org/10.1016/S1350-4487(99)00253-X.

Murray, A.S., Wintle, A.G., 2003. The single aliquot regenerative dose protocol: potential for improvements in reliability. Radiat. Meas. 37, 377–381. https://doi.org/10.1016/S1350-4487(03)00053-2.

Ortega, M., Sánchez, E., Gutiérrez, C., Molina, M.O., López-Franca, N., 2022. Regional winds over the Iberian Peninsula (Cierzo, Levante and Poniente) from high-resolution COSMO-REA6 reanalysis. Int. J. Climatol. 43, 1013–1033. https://doi.org/10.1002/joc.7860.

PAGES, Past Interglacials Working Group, 2016. Interglacials of the last 800,000 years. Rev. Geophys. 54, 162–219. https://doi.org/10.1002/2015RG000482.

Palacios, D., Hughes, P.D., Fletcher, W.J., Jomelli, V., Tanarro, L.M., 2024. Quaternary interglacials. The Holocene 2024, 37–49. https://doi.org/10.1016/B978-0-323-99712-6.00030-1.

Parés, J.M., Duval, M., Soria-Jáuregui, A., González-Amuchástegui, M.J., 2021. First chronological constraints for the high terraces of the upper Ebro catchment. Quaternary 4, 25. https://doi.org/10.3390/quat4030025.

Parton, A., Clark-Balzan, L., Parker, A.G., Preston, G.W., Sung, W.W., Breeze, P.S., Leng, M.J., Groucutt, H., White, T.S., Alsharekh, A., Petraglia, M.D., 2018. Middle-late quaternary palaeoclimate variability from lake and wetland deposits in the Nefud Desert, northern Arabia. Quat. Sci. Rev. 202, 78–97. https://doi.org/10.1016/j.quascirev.2018.10.010.

Plata, J.M., Rodríguez-Ochoa, R., Balasch, C., Boixadera, J., Poch, R.M., 2019. Loess source areas and spatial distribution in the lower Ebro Valley. Geophys. Res. Abstr. 21. https://doi.org/10.13140/RG.2.2.35927.24482. EGU2019-18998-1.

Plata, J.M., Rodríguez-Ochoa, R., Preusser, F., Boixadera, J., Balasch, J.C., Antúnez, M., Poch, R.M., 2021. Red soils in loess deposits of the eastern Ebro Valley. Catena 204, 105430. https://doi.org/10.1016/j.catena.2021.105430.

Poch, R.M., Rodríguez-Ochoa, R., Artieda, O., Balasch, J.C., Boixadera, J., 2021. Silt-sized sediments and gypsum on surface formations in the Ebro Basin: a disambiguation of the term "gypsiferous silts". Geol. Acta 19 (8), 1–21. https://doi.org/10.1344/GeologicaActa2021.19.8.

Prescott, J.R., Hutton, J.T., 1994. Cosmic ray contributions to dose rates for luminescence and ESR dating: large depths and long term time variations. Radiat. Meas. 23, 497–500. https://doi.org/10.1016/1350-4487(94)90086-8.

Quirantes, J., 1969. Estudio sedimentológico y estratigráfico del terciario continental de los Monegros. Universidad de Granada, Tesis doctoral, p. 200.

Railsback, L.B., Gibbard, P.L., Head, M.J., Voarintsoa, N.R.G., Toucanne, S., 2015. An optimized scheme of lettered marine isotope substages for the last 1.0 million years, and the climatostratigraphic nature of isotope stages and substages. Quat. Sci. Rev. 111, 94–106. https://doi.org/10.1016/j.quascirev.2015.01.012.

Ramsar Convention Secretariat, 2010. Ramsar Handbooks for the Wise Use of Wetlands, 4 1. Ramsar Convention Secretariat, Gland (Switzerland), p. 56.

Roberts, N., Reed, J.M., 2009. Lakes, wetlands, and Holocene environmental change. In: Woodward, J.C. (Ed.), The Physical Geography of the Mediterranean. Oxford University Press, Oxford, pp. 255–286.

Rodríguez-Santalla, I., Gómez-Ortiz, D., Muñoz-Pérez, J.J., 2025. Review of the internal structure of a climbing dune. The case of the Valdevaqueros dune (Caádiz, Spain). Front. Mar. Sci. 12, 1568474. https://doi.org/10.3389/fmars.2025.1568474.

Roffet-Salque, M., Marciniak, A., Valdes, P.J., Pawlowska, K., Pyzel, J., Czeniak, L., Krüger, M., Neil Roberts, C., Piter, S., Evershed, R.P., 2018. Evidence for the impact of the 8.2-ky BP climate event on near eastern early farmers. Proc. Natl. Acad. Sci. 115 (35). https://doi.org/10.1073/pnas.1803607115, 201803607.

Sánchez, F.J., Lastra, J. (Eds.), 2011. Guía metodológica para el desarrollo del Sistema Nacional de Cartografía de Zonas Inundables. Madrid, Ministerio de Medio Ambiente, y Medio Rural y Marino 324. Available at: https://www.miteco.gob.es/content/dam/miteco/es/agua/temas/ges-tion-de-los-riesgos-de-inundacion/guia_snczi_baja_optimizada_tcm30-422920.pdf.

Sánchez-Navarro, J.A., Pérez, A., Coloma, P., Martínez-Gil, F.J., 1998. Combined effects of groundwater and aeolian processes in the formation of the northernmost closed saline depressions of Europe, north-East Spain. Hydrol. Process. 12, 813–820. https://doi.org/10.1002/(SICI)1099-1085(19980430)12:5<813::AID-HYP629>3.0.CO;2-P.

Sancho, C., Calle, M., Peña-Monné, J.L., Duval, M., Oliva-Urcia, B., Pueyo, E.L., Benito, G., Moreno, A., 2016. Dating the earliest Pleistocene alluvial terrace of the Alcanadre River (Ebro Basin, NE Spain): insights into the landscape evolution and involved processes. Quat. Int. 407, 86–95. https://doi.org/10.1016/j.quaint.2015.10.050.

Schoeneberger, P.J., Wysocki, D.A., Benham, E.C., Soil Survey Staff, 2012. Field Book for Describing and Sampling Soils, Version 3.0. Natural Resources Conservation Service, National Soil Survey Center, Lincoln, NE. Available at: https://www.nrcs.usda.gov/sites/default/files/2025-04/Field-Book-for-Describing-and-Sampling-Soils-v4.pdf.

Shaw, P., Bryant, R., 2011. Pans, playas and salt lakes. In: Thomas, D. (Ed.), Arid Zone Geomorphology. John Wiley and Sons, pp. 373–401.

Smith, M., Segeren, A., Santos Pereira, L., Perrier, A., Allen, R., 1990. Report on the Expert Consultation on Procedures for Revision of FAO Guidelines for Prediction of Crop Water Requirements, 68, pp. ed. FAO, Rome, Italy. Available at: https://openknowledge.fao.org/handle/20.500.14283/cb7185en.

Søe, N.E., Kroon, A., Vad Odgaard, B., Lykke-Andersen, H., Much Kristiansen, S., 2018. Bathymetric control of Holocene spit migration in a lacustrine environment. Holocene 28 (8), 1245–1254. https://doi.org/10.1177/0959683618771.

Soil Survey Staff (SSS), 2022. Keys to Soil Taxonomy, 13th ed. USDA - Natural Resources Conservation Service, Washington DC, p. 410. Available at: https://www.nrcs.usda.gov/sites/default/files/2022-09/Keys-to-Soil-Taxonomy.pdf.

Solà, J., Costa, M., Olivé, A., Simón, J.L., González, J.C., García, A., Hernández, A., 1997. Memoria Y Mapa geológico de España/Report and Geological Map of Spain, Escala/Scale 1:50.000. Hoja/Sheet 442, Caspe. Instituto Geológico y Minero de España, Madrid, p. 58.

Launder, B.E., Spalding, D.B., 1974. The numerical computation of turbulent flows. Comput. Methods Appl. Mech. Eng. 3, 269–289. https://doi.org/10.1016/0045-7825(74)90029-2.

Stoops, G., 2003. Guidelines for Analysis and Description of Soil and Regolith Thin Sections. Soil. Science Society of America, Inc., Madison, WI.

Tierra, M., Gracia, F.J., Rodríguez-Ochoa, R., Olarieta, J.R., Paniagua, P., García, E., Castañeda, C., 2024. Soils and geomorphology of "Salada de Chiprana" RAMSAR wetland, NE Spain [dataset]. Mendeley Data V1. https://doi.org/10.17632/ng7dmks479.1.

Timms, B.V., 1992. Lake Geomorphology. Gleneagles Publ, Adelaide, p. 180.

Torgersen, T., 1984. Wind effects on water and salt loss in playa lakes. J. Hydrol. 74 (137), 149. https://doi.org/10.1016/0022-1694(84)90145-8.

Torres-Guerrero, C.A., Álvarez, D., Preusser, F., Olarieta, J.R., Poch, R.M., 2023. Evolution of soil porosity in loess-palaeosol sequences of the Ebro Valley. NE Iberia. Catena 230, 107244. https://doi.org/10.1016/j.catena.2023.107244.

Torres-Guerrero, C.A., Álvarez, D., Preusser, F., Olarieta, J.R., Poch, R.M., 2024. Corrigendum to "evolution of soil porosity in loess-palaeosol sequences of the Ebro Valley, NE Iberia". Catena 236, 1072703. https://doi.org/10.1016/j.catena.2023.107703.

Tzedakis, P.C., 2009. Cenozoic climate and vegetation change. In: Woodward, J.C. (Ed.), The Physical Geography of the Mediterranean. Oxford University Press, Oxford, pp. 89–137.

United States Salinity Laboratory Staff, 1954. Diagnosis and improvement of saline and alkali soils. In: Agriculture Handbook 60. USDA, Washington DC. https://www.ars.usda.gov/ARSUserFiles/20360500/hb60_pdf/hb60complete.pdf.

Valdeolmillos-Rodríguez, A., Dorado-Valiño, M., Ruiz-Zapata, M.B., Alonso-Zarza, A.M., 2011. Middle Pleistocene variations in palaeoclimate, palaeoenvironment and vegetation of the las Tablas de Daimiel National Park (Spain). J. Quat. Sci. 26, 128–140. https://doi.org/10.1002/jqs.1440.

Valero-Garcés, B.L., Navas, A., Machin, J., Stevenson, T., Davis, B., 2000. Responses of a saline Lake ecosystem in a semiarid region to irrigation and climate variability: the history of Salada Chiprana, Central Ebro Basin. Spain. AMBIO 29 (6), 344–350. https://doi.org/10.1639/0044-7447(2000)029[0344:ROASLE]2.0.CO;2.

Van der Made, J., Lazagabaster, I.A., García-Medrano, P., Cáceres, I., 2025. Southernmost Eurasian record of reindeer (*Rangifer*) in MIS 8 at Galería (Atapuerca,

Spain): evidence of progressive southern expansion of glacial fauna across climatic cycles. Quaternary 8, 43. https://doi.org/10.3390/quat8030043.
Van Zuidam, R.A., 1976. Geomorphological Development of the Zaragoza Region. International Institute for Aerial Survey and Earth Sciences (ITC), Enschede, Spain, p. 209.
Visher, G., 1969. Grain size distribution and depositional processes. J. Sediment. Petrol. 39, 1074–1106. https://doi.org/10.1306/74D71D9D-2B21-11D7-8648000102C1865D.
Wang, J., Jiang, Z., Xian, B., Chen, J., Wang, X., Xu, W., Liu, H., 2017. A method to define the palaeowind strength from lacustrine parameters. Sedimentology 65 (2), 461–491. https://doi.org/10.1111/sed.12388.
Wright Jr., H.E., 1964. Origin of the lakes in the Chuska Mountains, Northwestern New Mexico. Geol. Soc. Am. Bull. 75, 589–598. https://doi.org/10.1130/0016-7606(1964)75[589:OOTLIT]2.0.CO;2.